Atmospheric chemistry and aerosols

Composition of planetary atmospheres

Object	Mass (kilograms)	Carbon Dioxide	Nitrogen	Oxygen	Argon	Methane	Sodium	Hydrogen	Helium	Other
Sun	3.0×10^{30}							71%	26%	3%
Mercury	1000			42%			22%	22%	6%	8%
Venus	4.8×10^{20}	96%	4%							
Earth	1.4×10^{21}		78%	21%	1%					<1%
Moon	100,000				70%		1%		29%	
Mars	2.5×10^{16}	95%	2.7%		1.6%					0.7%
Jupiter	1.9×10^{27}							89.8%	10.2%	
Saturn	5.4×10^{26}							96.3%	3.2%	0.5%
Titan	9.1×10^{18}		97%			2%				1%
Uranus	8.6×10^{25}					2.3%		82.5%	15.2%	
Neptune	1.0×10^{26}					1.0%		80%	19%	
Pluto	1.3×10^{14}	8%	90%			2%				

from NASA HP

photosynthesis

$$6\,CO_2 + 6H_2O + \text{energy} \longrightarrow C_6H_{12}O_6 + 6\,O_2$$

Need for understanding chemistry

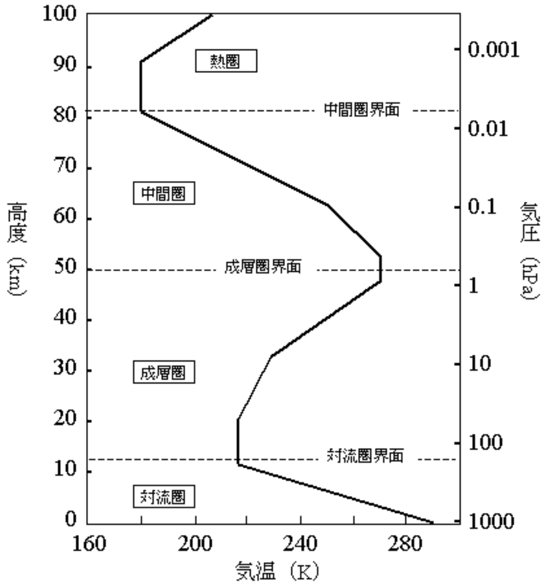

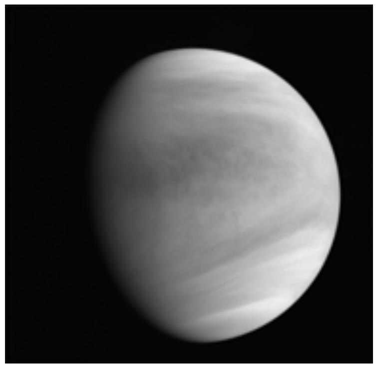

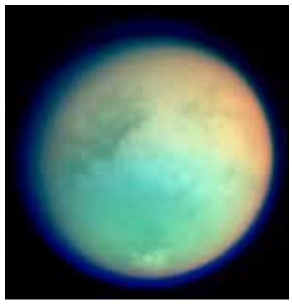

Chemical kinetics

A reaction between reactants A and B to form product C:

A + B → C reaction rate = *k* [A] [B]

A + B + M → C + M reaction rate = *k* [A] [B] [M]

M is any inert molecule that can remove the excess energy.

k is the reaction rate constant that usually depends on the temperature as (Arrhenius equation):

$$k = A \exp\left(-\frac{E_a}{k_B T}\right)$$

where E_a is the activation energy.

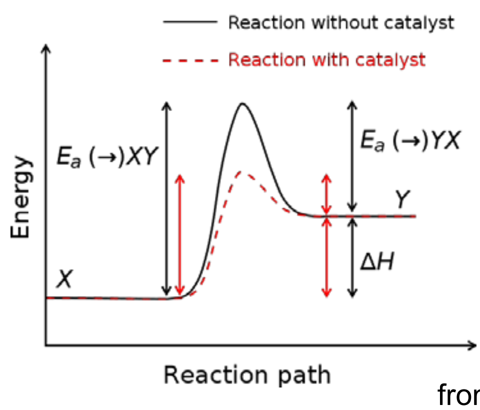

from Wikipedia

Production and destruction of ozone

Chapman theory

$O_2 + hv \rightarrow 2O$
$O + O_2 + M \rightarrow O_3 + M$

$3O_2 \rightarrow 2O_3$

$O_3 + hv \rightarrow O + O_2$
$O + O_3 \rightarrow 2O_2$

$2O_3 \rightarrow 3O_2$

- Chapman theory predicts an ozone amount of several times larger than the observations.
- Other loss mechanisms are required.

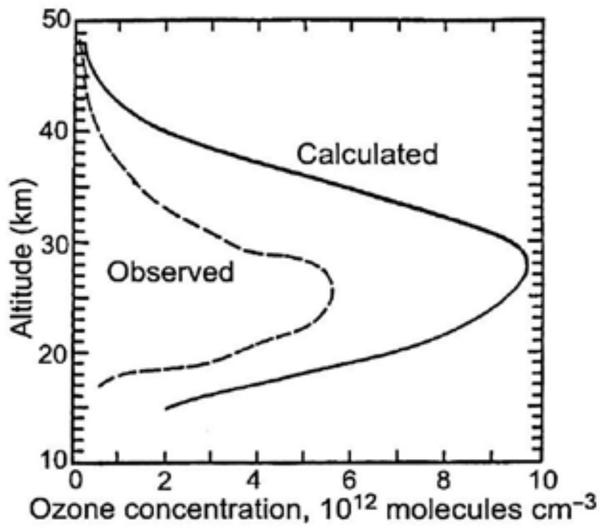

Figure 3.1 An ozone profile calculated with the Chapman reactions at the equator overestimates the ozone compared with observations over Panama at 9° N on November 13, 1970. The reason is that natural catalysts that destroy ozone are omitted from the oxygen-only Chapman reactions. (Adapted from Seinfeld and Pandis (1998). Reproduced with permission. Copyright 1998, John Wiley and Sons.)

Catling & Kasting (2017)

Catalytic cycles

$X + O_3 \rightarrow XO + O_2$
$XO + O \rightarrow X + O_2$

$O + O_3 \rightarrow 2O_2$

X : Free radical such as OH, NO, Cl, Br

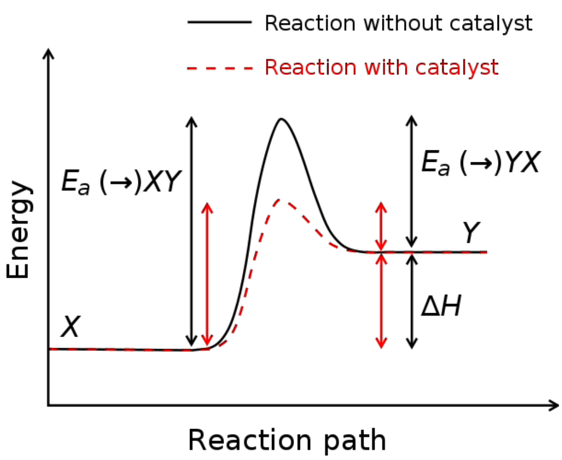

The net result of the catalytic cycle is to remove O and O_3 rapidly.

Stability of CO_2 atmosphere

$$
\begin{array}{c}
2(CO_2 + h\nu \rightarrow CO + O) \\
O + O + M \rightarrow O_2 + M \\
\hline
\text{Net: } 2CO_2 \rightarrow 2CO + O_2
\end{array}
$$

The reaction $CO + O \rightarrow CO_2$ is very slow (spin forbidden).
Mars and Venus atmospheres are expected to be converted to CO and O_2 in 6000 years.

Catalytic cycle on Mars ?

On Mars, OH radicals are thought to play crucial roles.

$$H_2O + h\nu \rightarrow OH + H$$

McElroy and Donahue [1972]

Production of OH

$$H + O_2 + M \rightarrow HO_2 + M$$
$$\boxed{HO_2} + O \rightarrow \boxed{OH} + O_2$$

Production of CO_2

$$CO + \boxed{OH} \rightarrow CO_2 + H,$$

Net reaction

$$CO + O + M \rightarrow CO_2 + M.$$

Parkinson and Hunten [1972]

Production of OH

$$2(H + O_2 + M \rightarrow HO_2 + M)$$
$$HO_2 + HO_2 \rightarrow H_2O_2 + O_2$$
$$\boxed{H_2O_2} + h\nu \rightarrow \boxed{OH} + OH$$

Production of CO_2

$$2(CO + \boxed{OH} \rightarrow CO_2 + H),$$

Net reaction

$$2CO + O_2 \rightarrow 2CO_2.$$

Atreya and Gu (1994)

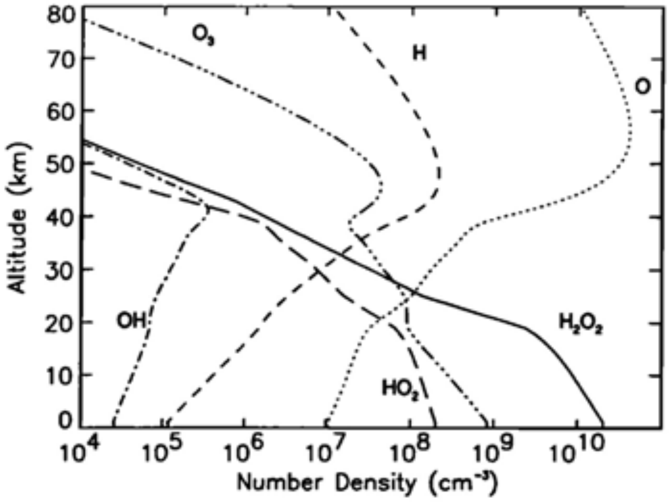

Figure 8. Distribution of key constituents based on the nominal model ($H_2O = 150$ ppm, $K = 10^6\,cm^2 s^{-1}$, $\tau_d = 0.4$; see text).

Photochemistry is effective even near the surface on Mars because of the thin atmosphere.

Catalytic cycle on Venus?

Cl radicals are thought to play crucial roles.

$$\begin{array}{lr} Cl + CO + M \rightarrow \boxed{ClCO} + M & (27) \\ ClCO + O \rightarrow CO_2 + Cl & (28) \\ \hline \text{Net: } CO + O \rightarrow CO_2 & (E) \end{array}$$

$$\begin{array}{lr} Cl + CO + M \rightarrow \boxed{ClCO} + M & (27) \\ ClCO + O_2 + M \rightarrow \boxed{ClC(O)OO} + M & (29) \\ ClC(O)OO + Cl \rightarrow CO_2 + ClO + Cl & (30) \\ ClO + O \rightarrow Cl + O_2 & (26) \\ \hline \text{Net: } CO + O \rightarrow CO_2 & (G1) \end{array}$$

$$\begin{array}{lr} Cl + CO + M \rightarrow \boxed{ClCO} + M & (27) \\ ClCO + O_2 + M \rightarrow \boxed{ClC(O)OO} + M & (29) \\ ClC(O)OO + O \rightarrow CO_2 + O_2 + Cl & (31) \\ \hline \text{Net: } CO + O \rightarrow CO_2 & (G2) \end{array}$$

$$\begin{array}{lr} Cl + CO + M \rightarrow \boxed{ClCO} + M & (27) \\ ClCO + O_2 + M \rightarrow \boxed{ClC(O)OO} + M & (29) \\ ClC(O)OO + h\upsilon \rightarrow CO_2 + ClO & (32) \\ ClO + O \rightarrow Cl + O_2 & (26) \\ \hline \text{Net: } CO + O \rightarrow CO_2 & (G3) \end{array}$$

Mills et al. (2007)

Mills et al. (2007)

Vega-2 X-ray spectrometer result
(Andreychikov et al. 1987)

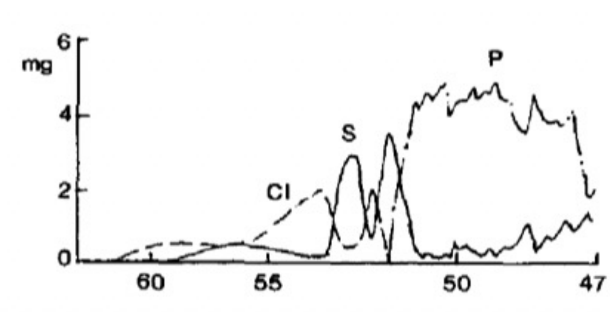

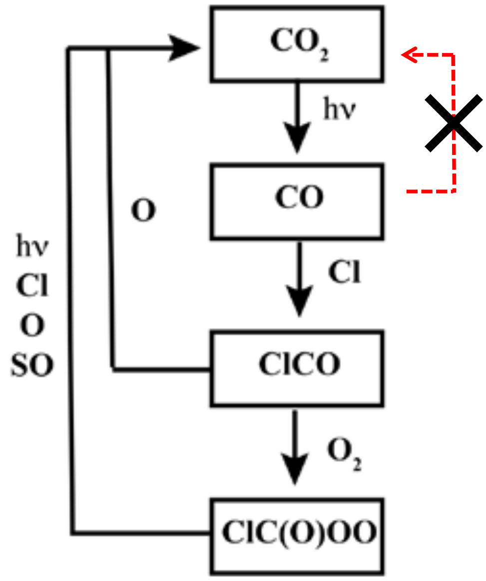

Figure 3. Schematic showing primary pathways for production of CO_2 via chlorine chemistry. The reaction $ClCO + O \rightarrow CO_2 + Cl$ accounts for 15 and 20% of the column total CO_2 production in the $+0.5\sigma$ and $+2.0\sigma$ models from Table 5, respectively.

ClCO, $ClCO_3$ and other key species have never been observed.

Clouds/aerosols

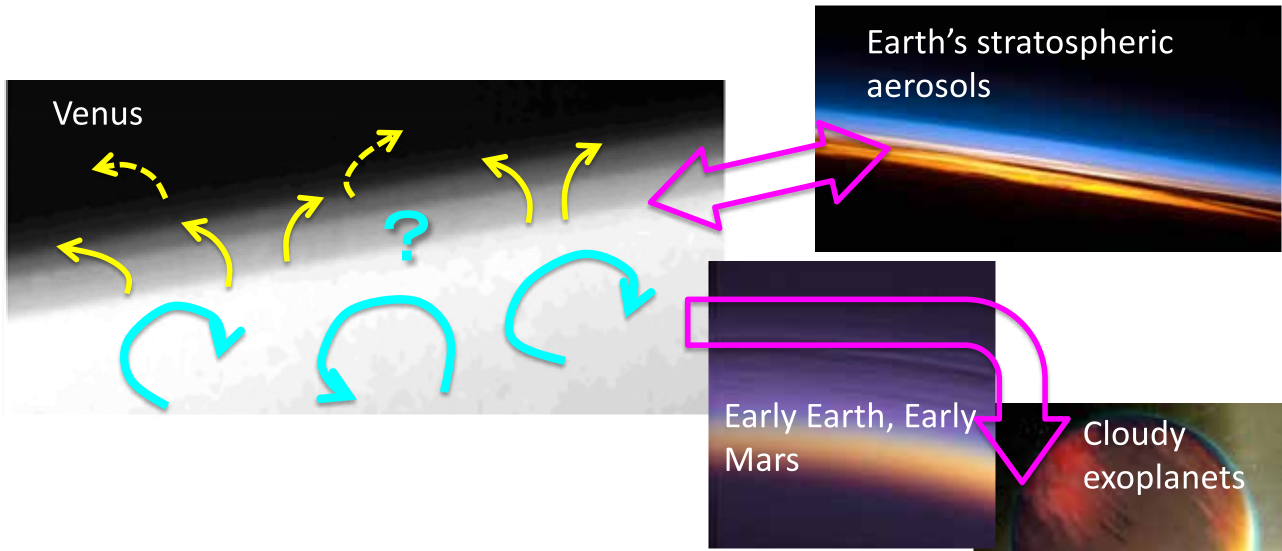

- Controlling planetary albedo
- Scattering greenhouse effect
- Regulating atmospheric species transported to the upper atmosphere

Cloud formation

Andrews (2010)

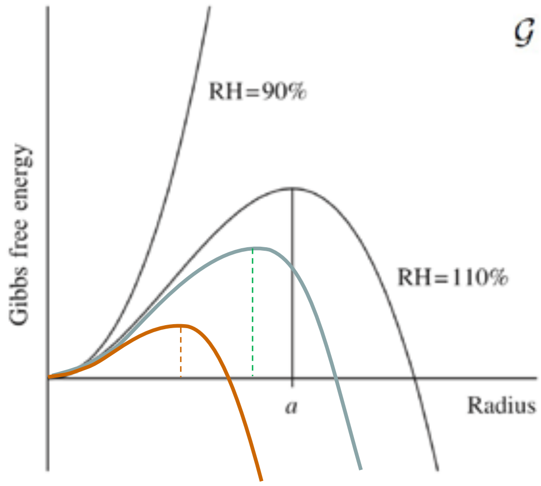

Gibbs free energy

$$\mathcal{G} - \mathcal{G}_0 = -\frac{4}{3}\pi a^3 \rho_l R_v T \ln\left(\frac{e}{e_s(T)}\right) + 4\pi a^2 \gamma$$

a : radius of droplet
e : partial vapor pressure
e_s : saturation vapor pressure
γ : surface tension
ρ_l : liquid density
R_v : gas constant
T : temperature

Pure water:

equilibrium radius	relative humidity(RH)
0.01 µm	→ 112%
0.1 µm	→ 101%
flat surface	→ 100%

If a cloud droplet is to survive, it must somehow attain a radius greater than the equilibrium radius a corresponding to the ambient relative humidity
→ Need for condensation nucleus

Role of soluble cloud condensation nuclei (CCN)

Andrews (2010)

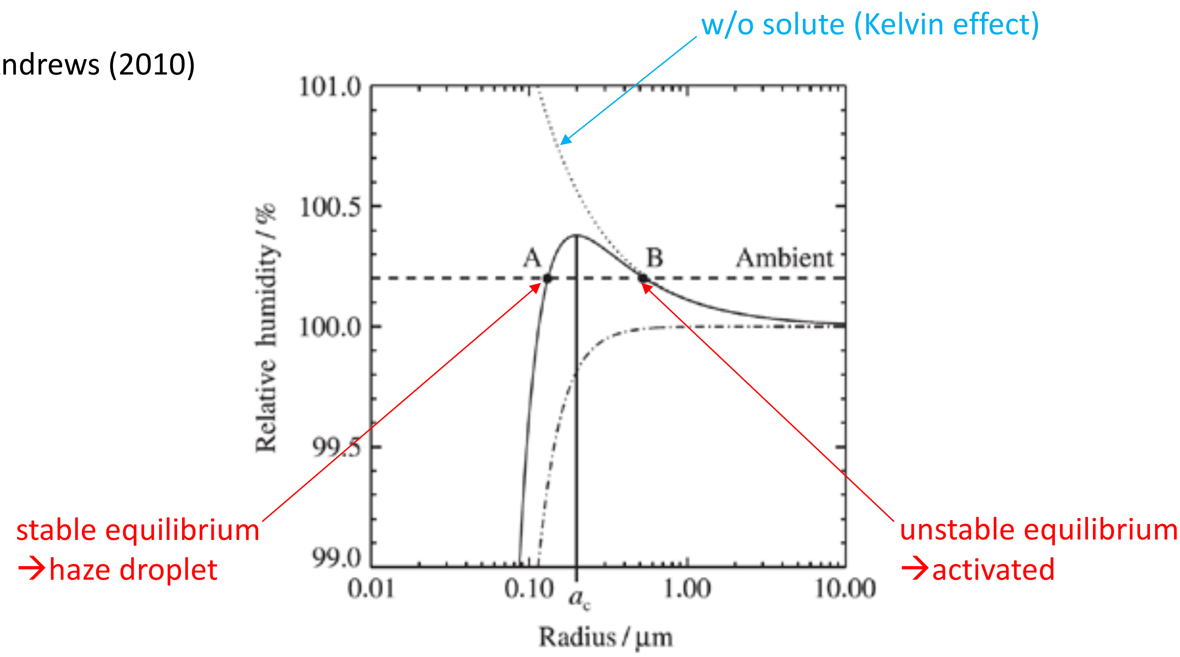

The Köhler curve (solid) for the relative humidity RH = e/e_s over a spherical droplet of water containing solute, as a function of droplet radius a, at 5 °C. The solute is taken to be 10^{-19} kg of NaCl. The Kelvin factor is given by the dotted curve and the Raoult factor is given by the dash-dotted curve. The thick horizontal dashed line and points A and B are discussed in the text.

Composition of CCN

Example of the composition of ice forming nuclei in Earth's troposphere (Pruppacher & Klett 1997)

TABLE 9.6
Composition of ice forming nuclei derived from aerosolized soil in Montana (from Rosinski *et al.*, 1981).

Chemical composition	Aerosol particles number	Aerosol particles %	Ice-forming nuclei active at temperature −12°C number	−12°C %	−15°C number	−15°C %	−20°C number	−20°C %
Clay minerals:								
montmorillonite	194	24	28	18	17	13	41	28
feldspar	287	36	74	48	41	32	54	38
illite	163	20	37	24	39	31	28	19
miscellaneous	27	3	8	5	19	15	10	7
Organic particles	139	17	7	5	12	9	11	8
Number of particles: analyzed	810		154		128		144	
Mixed particles containing:								
NaCl	7		14	9	28	22	21	15
CuX	2		1		0		1	
$FeO_x.nH_2O$	-		7	5	12	9	11	8
Total	9		22	14	40	31	33	23

- The characteristics of CCN on other planets are totally unknown.
- Dust particles will serve as CCN on Mars.
- Galactic cosmic rays may also work. Cosmic rays increase small ions (charged molecules or charged small clusters of molecules) in the atmosphere, leading to increase in the nucleation rate of aerosol particles.

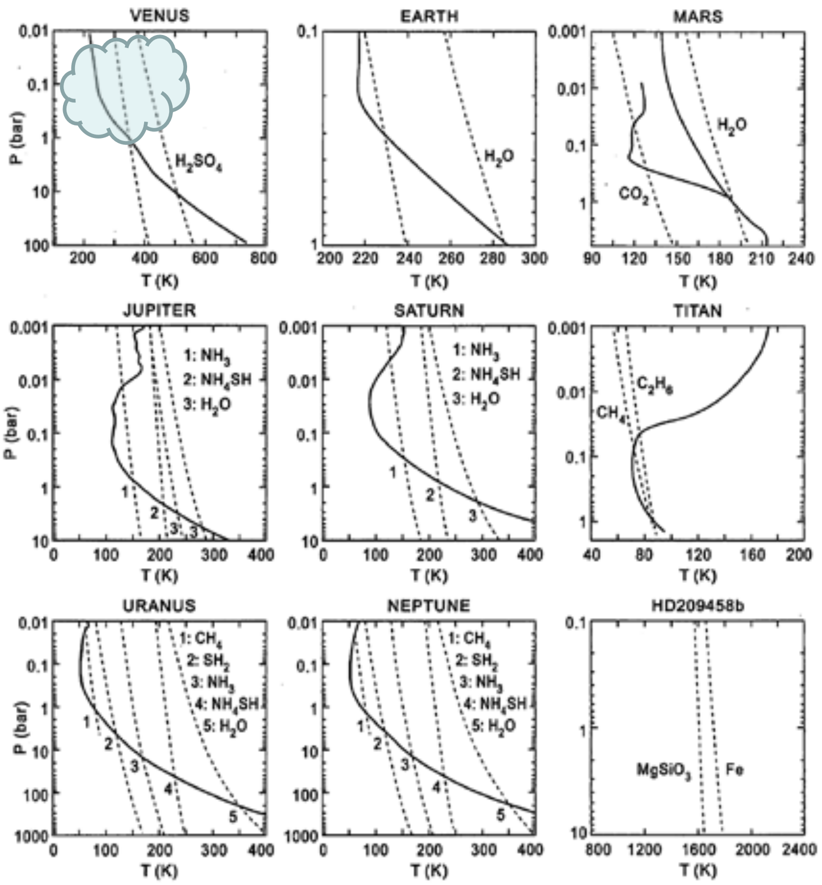

Catling & Kasting (2017)

The solid curves are the typical vertical profiles of pressure versus temperature. Dashed curves are the saturation vapor pressure curves for various condensables.

Particles condense when the partial pressure reaches the saturation vapor pressure.

H_2SO_4 clouds of Venus

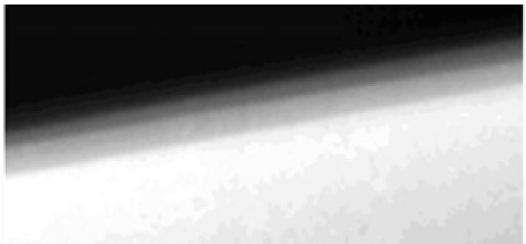

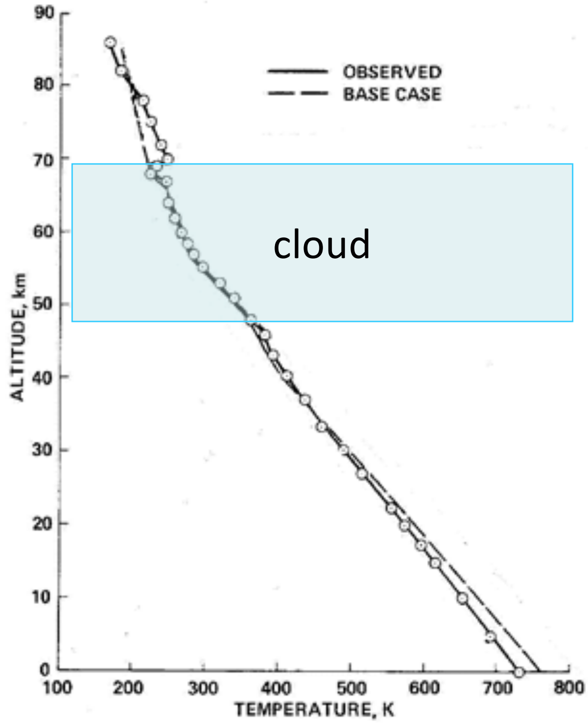

Fig. 2. Comparison between the observed temperature structure of Venus' lower atmosphere and that of several models, which are described in the main text.

- Solar energy flux reaching the Venus surface (17W/m^2) is much less than that of the Earth (168W/m^2).
- Greenhouse effect of massive CO_2 and small amount of H_2O explains the high temperature.

Pollack et al. (1980)

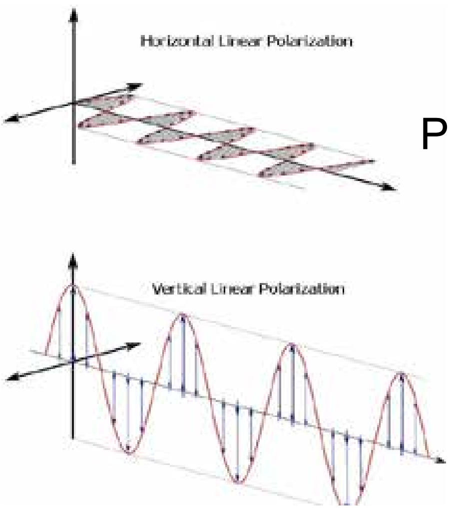

Polarization of sunlight reflected by Venus

Hansen & Hovenier (1974)

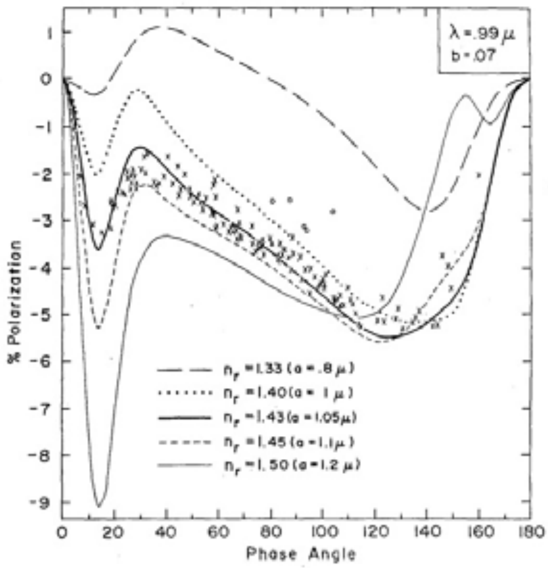

Fig. 7. Observations and theoretical computations of the polarisation of sunlight reflected by Venus at λ=0.99 μm. The observations were made with an intermediate bandwidth filter, the ×'s being obtained by Coffeen and Gehrels (1969) in 1959–67 and by Coffeen (cf. Dollfus and Coffeen, 1970) from 1967 to March 1969, and the O's being obtained by Coffeen (cf. Dollfus and Coffeen, 1970) in May–July, 1969. The theoretical curves are for spherical particles having the size distribution (8) with b=0.07. The different theoretical curves are for various refractive indices, the effective particle radius being selected in each case to yield closest agreement with the observations for all wavelengths.

Refractive index = 1.44

→consistent with H_2SO_4-H_2O solution

Effective radius ~ 1 μm

Microphysical properties of Venus clouds

- H_2SO_4-H_2O droplets with radii r < 5 μm
- Smallest mode (including sub-cloud haze) might be condensation nuclei whose composition is unknown.
- Size distribution is variable.

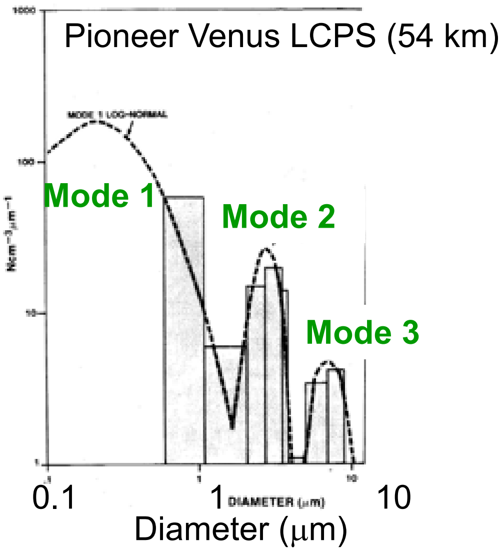

Venera-13 Lander

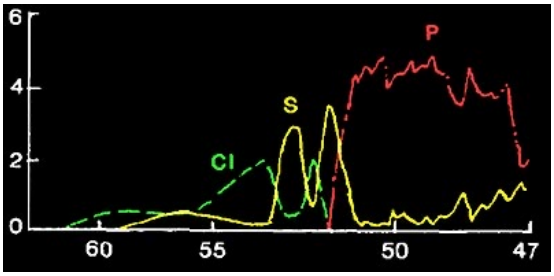

Cl ? S ? P ?

H_2SO_4 vapor in Venusian atmosphere

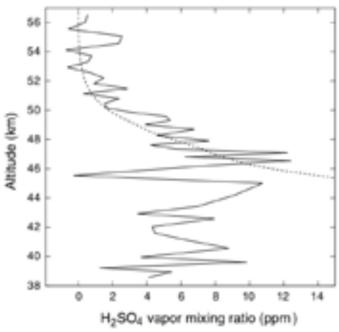

Imamura et al. (2017)

Measurement by radio occultation

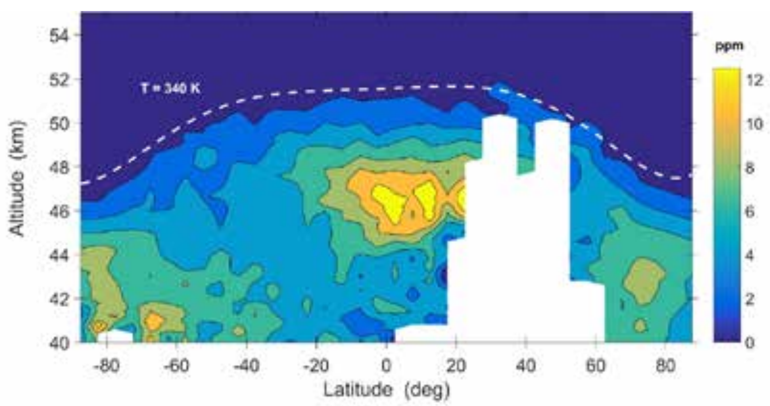

Fig. 9. Zonally and time-averaged sulfuric acid vapor distribution in the Venus lower atmosphere at all latitudes between the years 2006 and 2014 (lower panel). The hemispheres were subdivided into equal latitudinal bins of 5° each and H_2SO_4(g) profiles located within each bin were averaged to one mean profile. The number of data samples used for averaging is shown in the upper panel. The white dashed line in the lower panel shows the isotherm at T = 340 K derived from VeRa X-band radio occultation data from the same period. The H_2SO_4(g) values above this isotherm are generally as high as their uncertainties. Below the isotherm the values are higher than their uncertainties. The lack of measurements at northern mid latitudes between 20° and 60° is a consequence of the VEX orbit geometry.

Oschlisniok et al. (2021)

Sulfur-rich atmosphere: origin of H_2SO_4

SO_2 measurements by Vega landers

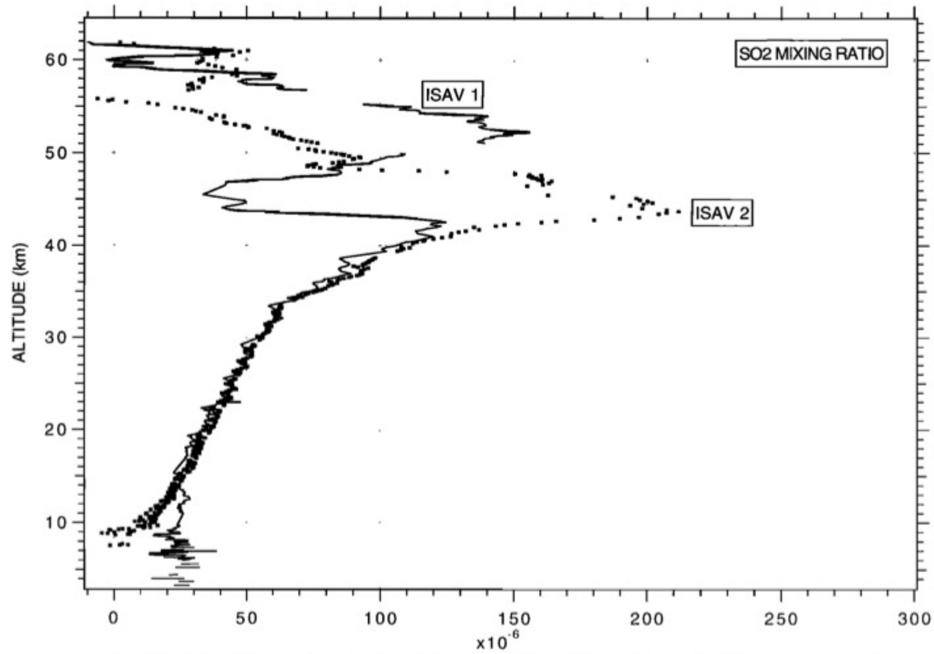

Figure 24. The SO_2 mixing ratio vertical profile retrieved for ISAV 2 (data points) is compared to that determined for ISAV 1. There is a large difference of structure above 40 km, while the profiles are nearly identical below 40 km. A peak of 210 ppm is observed at 43 km in the ISAV 2 data.

Bertaux et al. (1996)

Origin of clouds

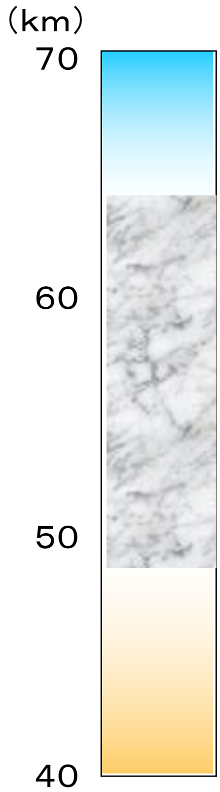

Photochemistry above clouds

Scenario #1 (Net reaction driven by catalytic cycles including ClOx, HOx, NOx)

$$2CO_2 + h\nu \rightarrow 2CO + O_2$$
$$CO + SO_2 + O_2 + h\nu \rightarrow CO_2 + SO_3$$
$$CO_2 + SO_2 + h\nu \rightarrow CO + SO_3$$

Scenario #2

$$SO_2 + h\nu \rightarrow SO + O$$
$$SO + h\nu \rightarrow S + O$$
$$SO_2 + O \rightarrow SO_3 \quad (\times 2)$$
$$3\,SO_2 + h\nu \rightarrow S + 2SO_3$$

- SO_3 rapidly reacts with H_2O: $SO_3 + H_2O \rightarrow H_2SO_4$
- Elemental sulfur (S) can serve as condensation nuclei.

Origin of clouds

H_2SO_4 vapor and H_2O vapor condenses onto condensation nuclei.

Growth of particles via collision during gravitational sedimentation

Evaporation around 50 km altitude due to high temperature

Thermochemistry below clouds (Net reaction driven by catalytic cycles

$H_2SO_4 \rightarrow H_2O + SO_3$

$SO_3 + CO \rightarrow CO_2 + SO_2$

$SO_3 + OCS \rightarrow CO_2 + (SO)_2$ etc

$H_2SO_4 + 4CO \rightarrow H_2O + 3CO_2 + OCS$

Retrieved vertical profiles

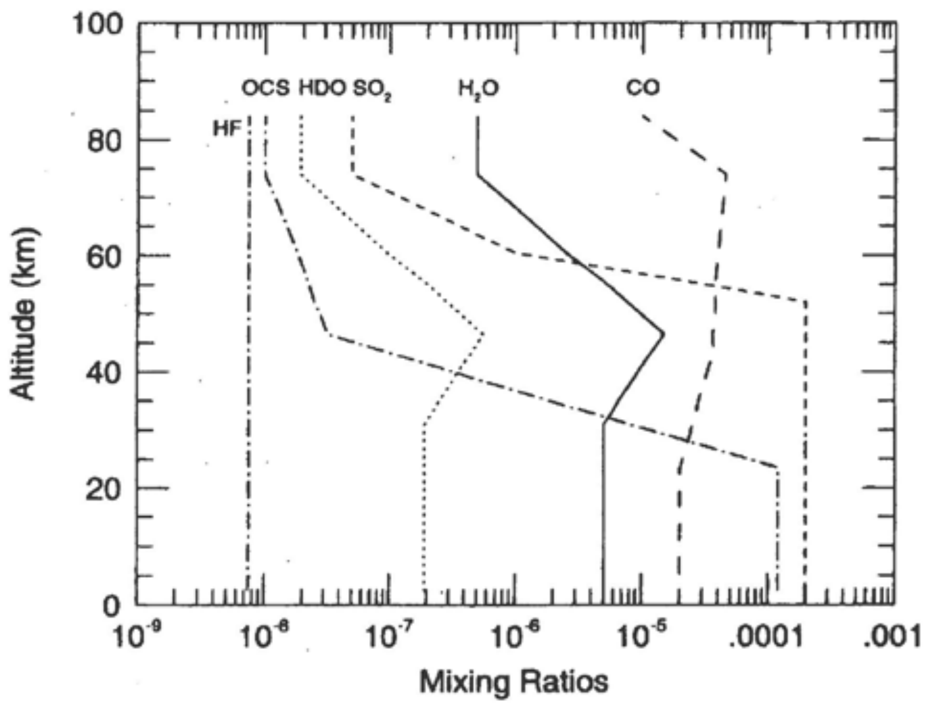

Pollack et al., Icarus 103, 1, 1993

Sedimentation of particles

Stokes velocity for a spherical particle

$$w_{\mathrm{sed}} = \frac{g\rho d^2}{18\eta}$$

g : gravitational acceleration
ρ : mass density of particle
d : diameter of particle
η : viscosity coefficient of air

comparable

Time constant of Hadley circulation
τ ~ 100 Earth days (from energy budget)
→ Vertical flow velocity ~ H/τ ~ 1 mm/s

Sedimentation velocity of droplets in Venusian atmosphere
(Imamura & Hashimoto 1998)

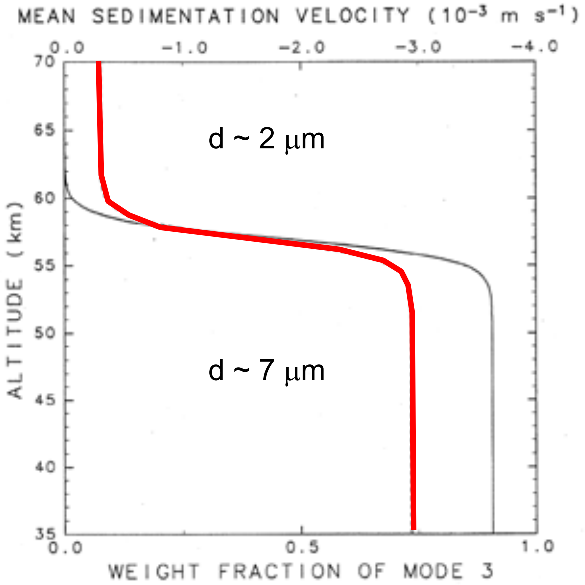

Figure 2. Fraction of Mode 3 particles by weight in the cloud (solid curve) adopted in the model after the observation by the Pioneer Venus particle size spectrometer, and the calculated mean sedimentation velocity W_{sed} (dashed curve). The cloud mass is assumed to be composed of particles of fixed radii, Mode 2 (r = 1.15 μm) and Mode 3 (r = 3.65 μm).

Possible role of planetary-scale meridional circulation

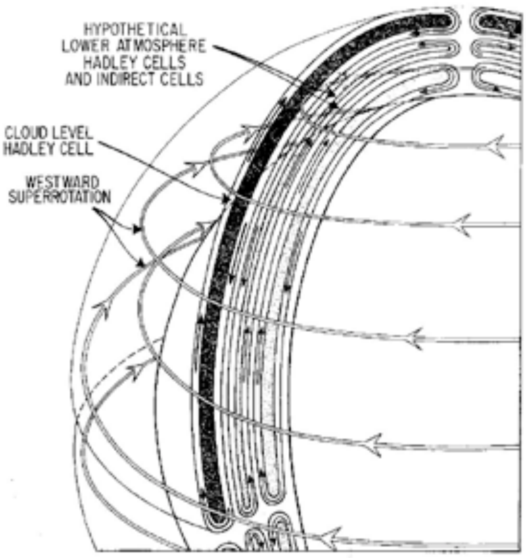

Schubert (1983)

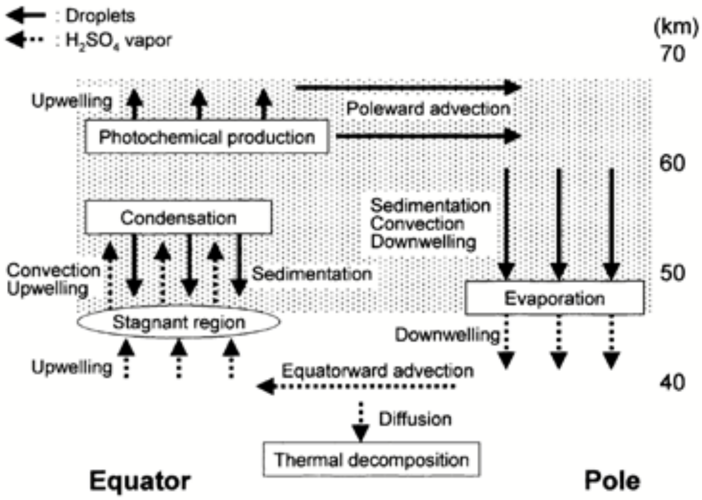

Imamura & Hashimoto (2001)

Lifecycle of Earth's stratospheric aerosols

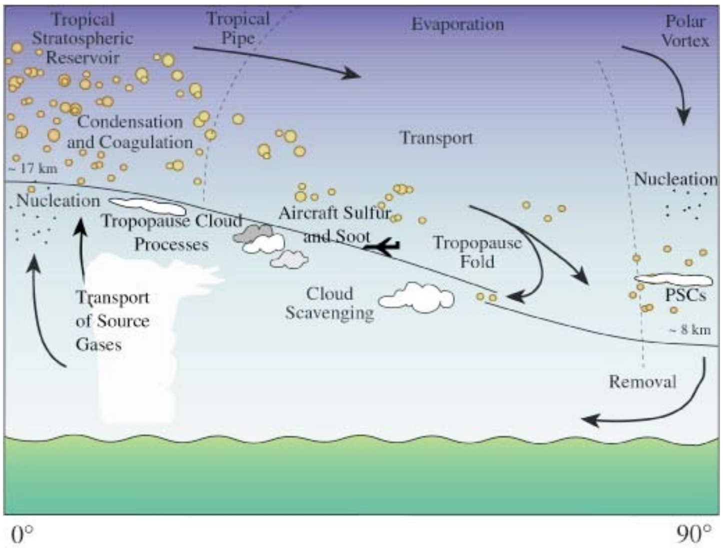

Hamill et al. (1997)

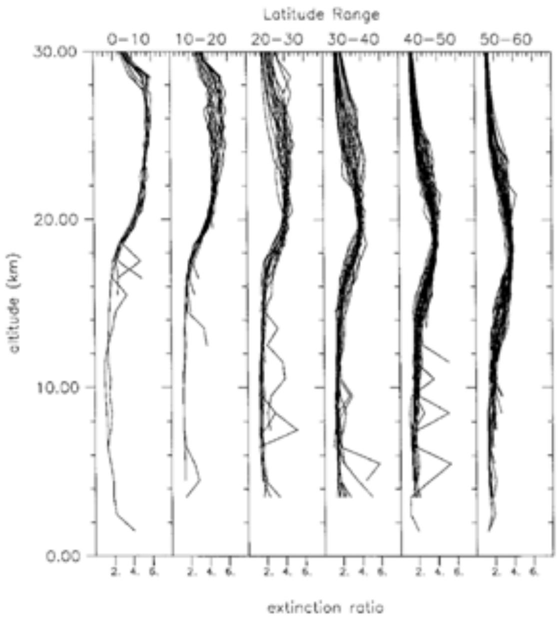

FIG. 9. Extinction ratios from the SAGE II satellite system in various latitude ranges. The extinction values were measured in April 1989 in the Southern Hemisphere. We have removed extinction ratios greater than 7 at lower altitudes for these are indications of tropospheric clouds.

Observed cloud morphology

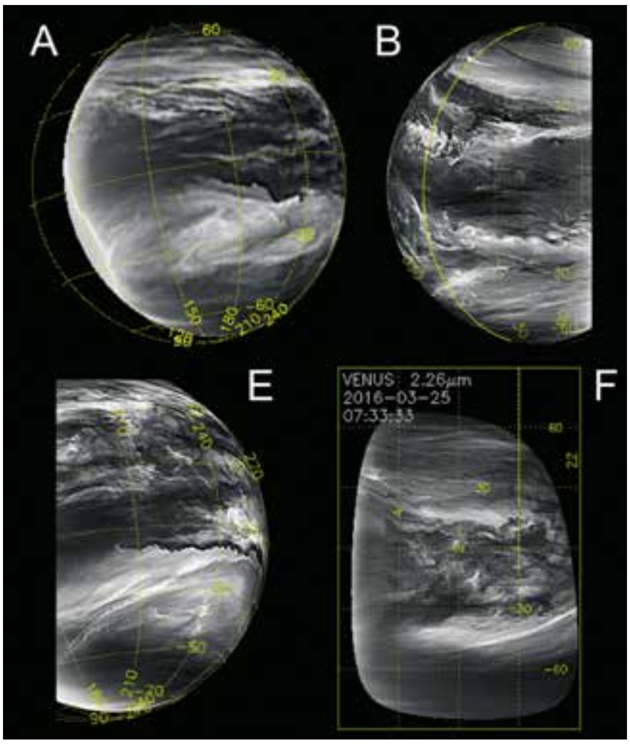

Peralta et al. (2018)

Equatorial dark clouds might be produced by large-scale upwelling near the cloud base

SO, SO_2 profiles above cloud observed by Venus Express solar occultations (Belyaev et al. 2011)

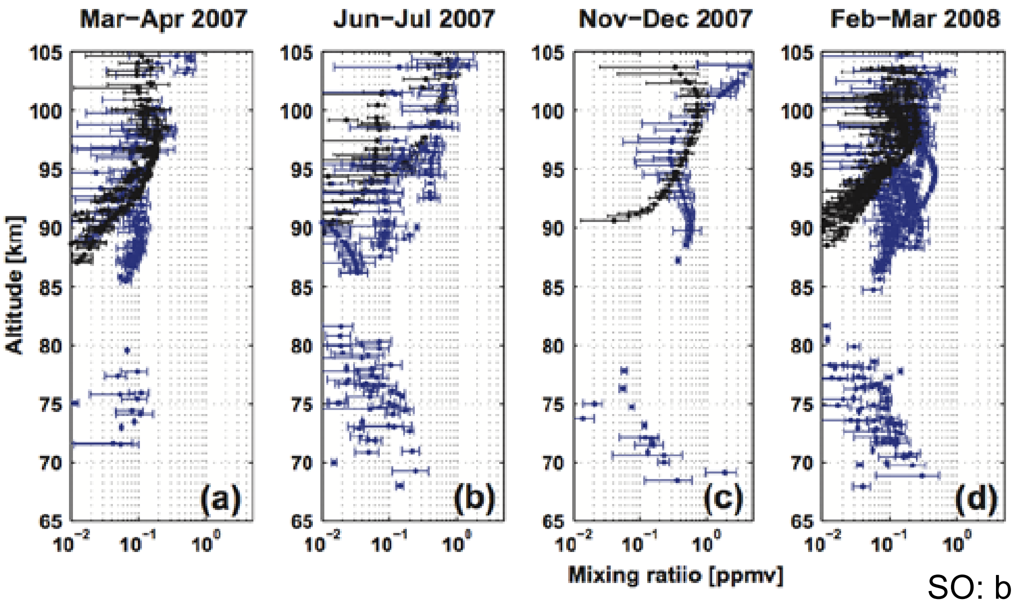

SO: black
SO_2: blue

- Enhancement at high altitudes cannot be explained by traditional photochemical models.

Chemical model of Venusian stratosphere (Zhang et al. 2012)

Artificial H_2SO_4 source added above 90 km:

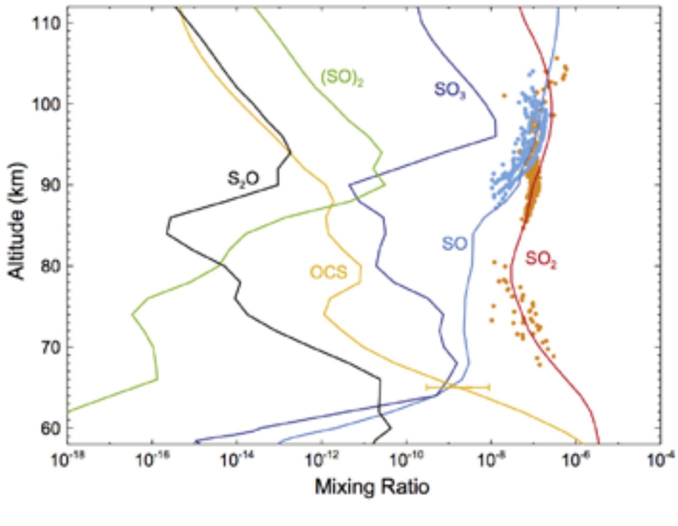

Fig. 8. Same as Fig. 2, for the sulfur oxides. The SO_2 and SO observations with errorbars are from the Belyaev et al. (2012). The temperature at 100 km is 165–170 K for the observations. The OCS measurement (0.3–9 ppb with the mean value of 3 ppb) is from Krasnopolsky (2010).

Transport of cloud particles to the upper atmosphere by winds ?
→ Open question

SO_2 (283 nm)

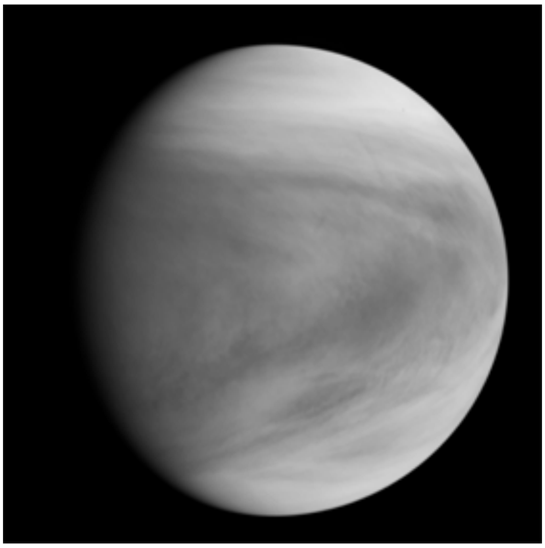

Unknown absorber (365 nm)

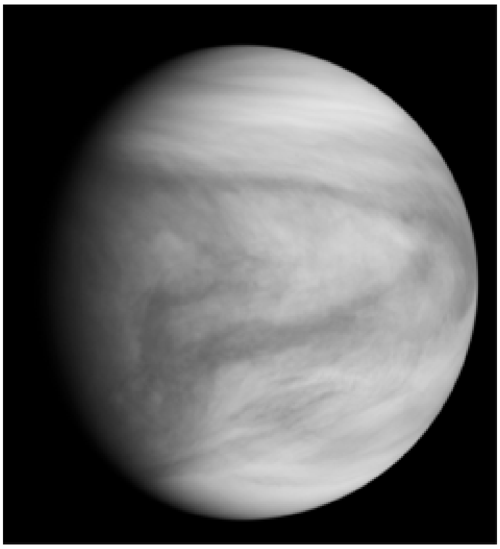

Venus is completely covered by clouds that are featureless in the visible but exhibit variable ultraviolet features.

Origin of visible-UV absorption

- Absorbing material at far UV (<320nm) is mostly SO_2
- Absorption at near UV (>320nm) is a mystery. Candidate species are S, S_2O_2, S_2O, $FeCl_2$, etc.

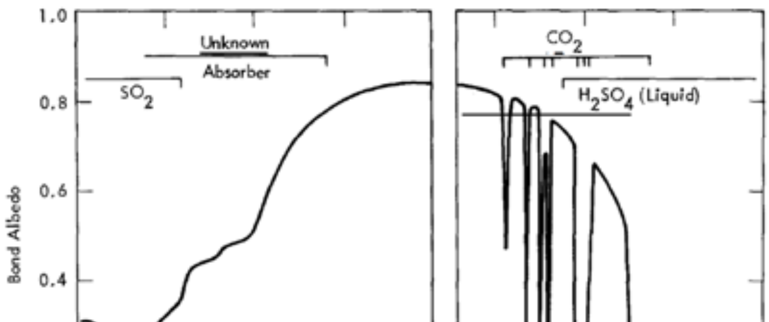

Moroz et al. (1985)

Figure 6-1. The Monochromatic Bond Albedo of Venus as a Function of Wavelength (Moroz, 1983 - Normalized to the Integrated Albedo A = 0.76). The points show the wavelength dependence of the maximum contrast between dark and light UV features (Coffeen, 1977).

Sulfur cycle in Venus's atmosphere

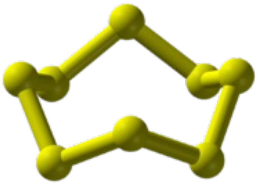

S_8

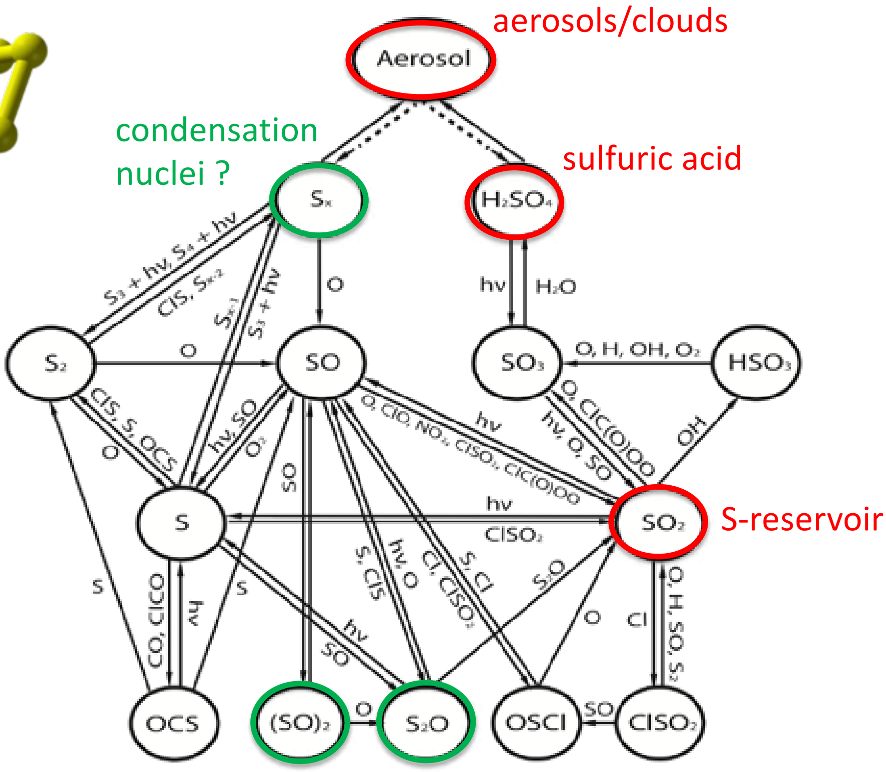

Zhang et al. (2012)

Variability of SO_2 above clouds

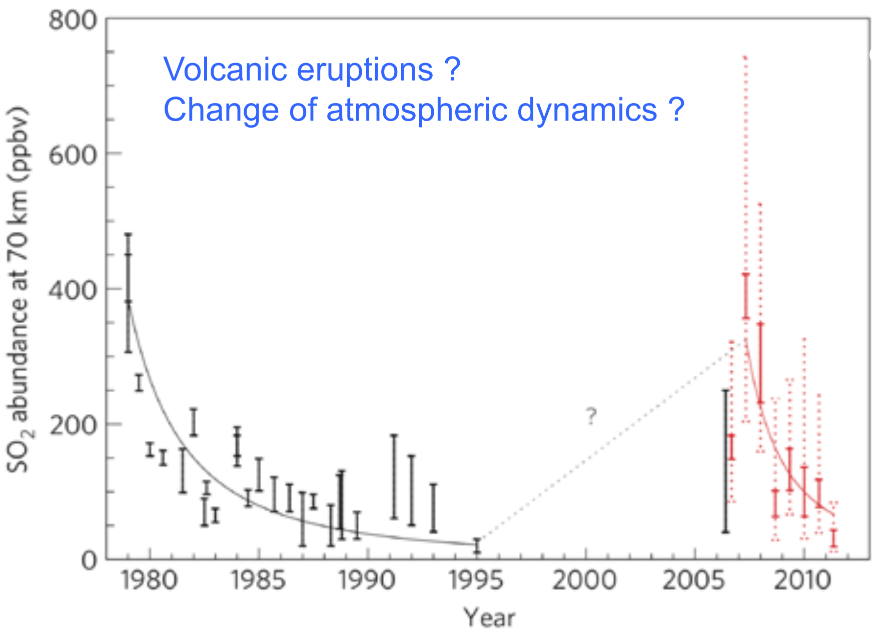

Marcq et al. (2013)

Figure 3 | More than thirty years of SO_2 measurements at Venus's cloud top. Black stands for previously published measurements[26]. Red stands for the 8-month moving average of the retrievals also shown in Fig. 1. Solid red error bars represent 1σ random uncertainty, and dotted red error bars represent measurement dispersion in each temporal bin.

Dust in the Martian atmosphere

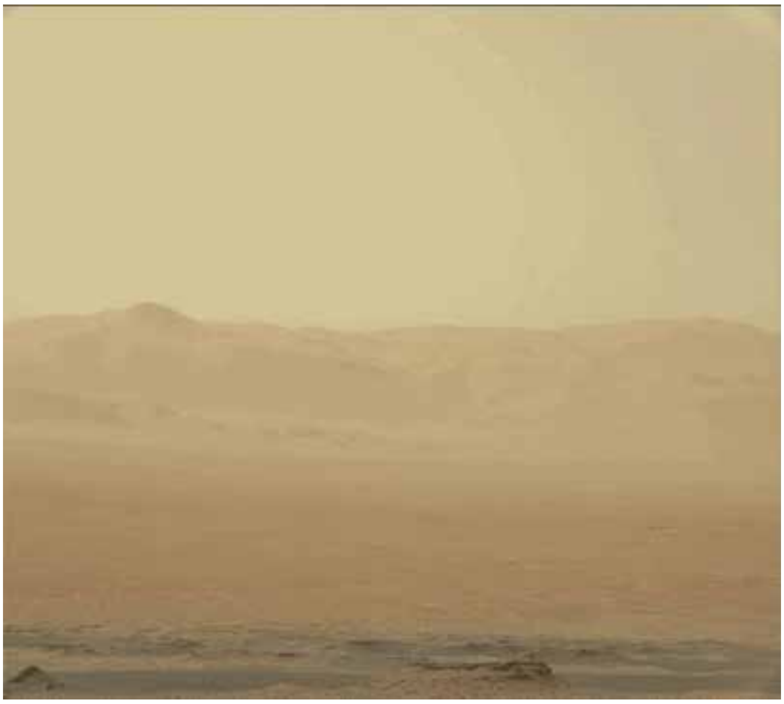

Martian dust storms span the entire planet, in June 2018.
The image was taken from the NASA's rover *Curiosity*

Dust in the Martian atmosphere

- Micrometer-sized small mineral particles float in the atmosphere with a background optical thickness of 0.1-0.5.
- The dust loading changes with time and space.
- The dust serves as a heat source in the atmosphere by absorbing sunlight.

Seasonal variation of optical thickness in infrared
(Smith et al. 2004)

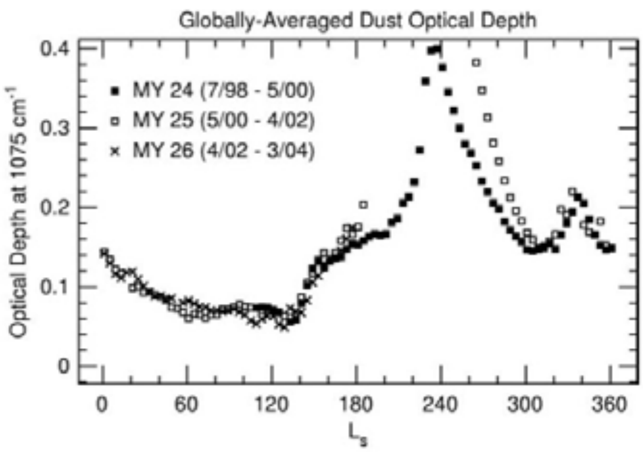

Fig. 7. Globally-averaged daytime (local time ~ 1400) dust optical depth at 1075 cm^{-1} (scaled to an equivalent 6.1-mbar pressure surface) as a function of season (L_s). Three martian years are represented: Mars Year 24 (MY 24) (■), MY 25 (□), MY 26 (×). During the planet-encircling dust storm of 2001 (MY 25), globally-averaged dust opacity reached 1.3 at $L_s = 205–215°$.

Seasons of Mars

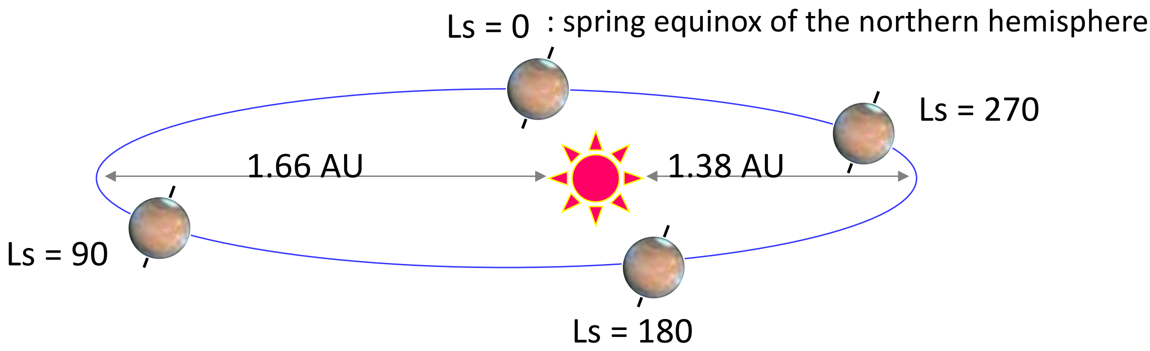

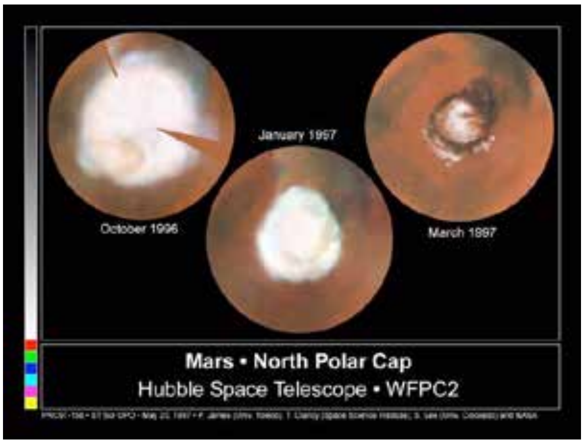

- 火星は公転軌道の離心率が大きいため季節変化が著しく南北非対称
- 南半球の夏に太陽までの距離が近くなる

Dust as a heat source

- Absorption of solar radiation
  - much stronger than the greenhouse effect of CO_2, which is only several kelvins
  - much stronger than cloud albedo effect and latent heat

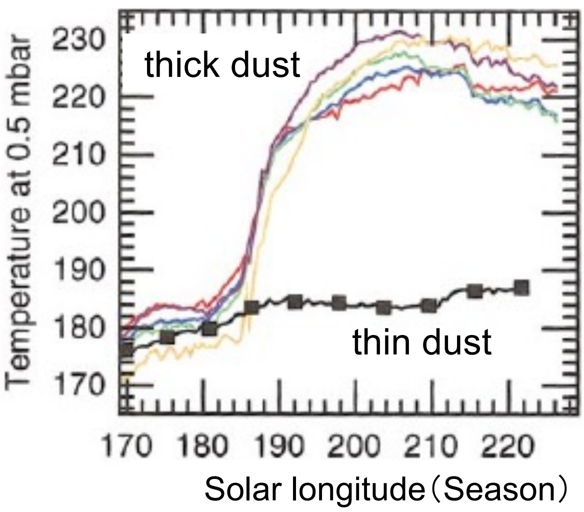

40 K difference between thick-dust year and thin-dust year

Smith et al. (2002)

Dust storms on Mars

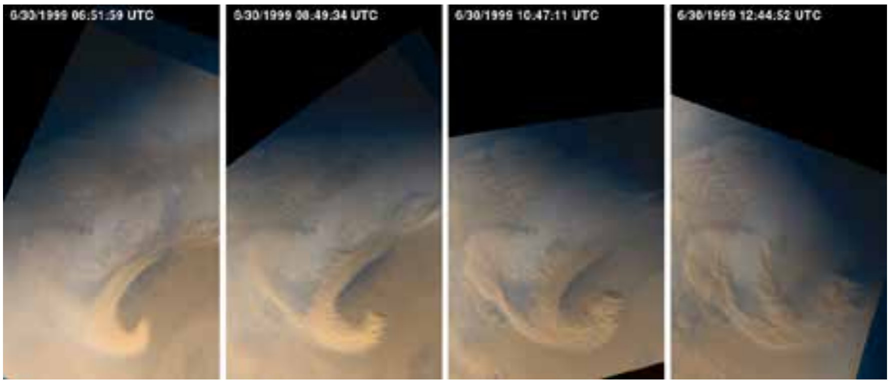

regional storm

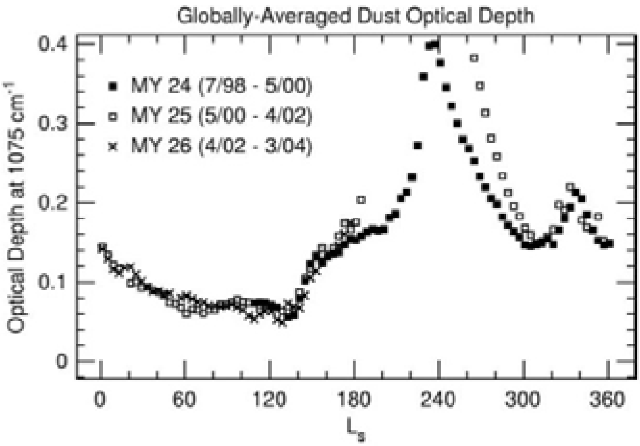

Seasonal variation of optical thickness in infrared
(Smith et al. 2004)

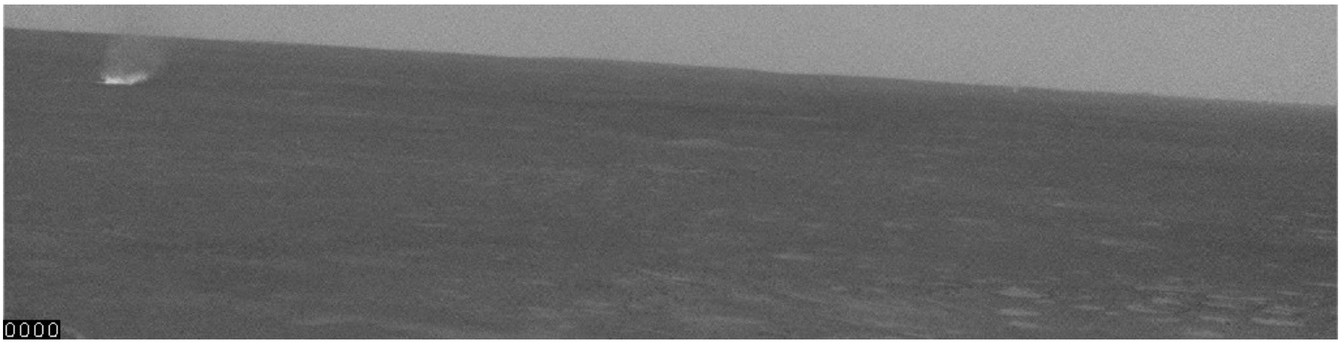

Dust devils

- Source of background atmospheric dust ?

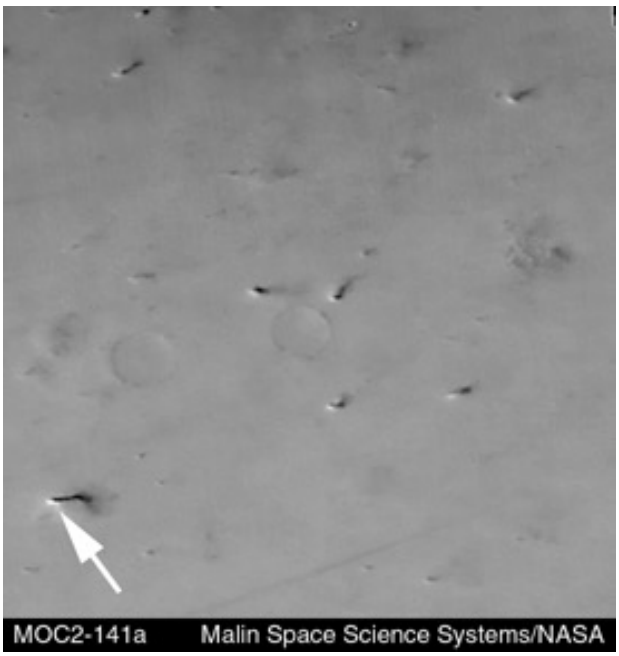

Distribution of atmospheric dust

- Origin of the “background” dust is unknown
- Maximum mixing ratio at 10−20 km altitudes

Smith et al. (2004)

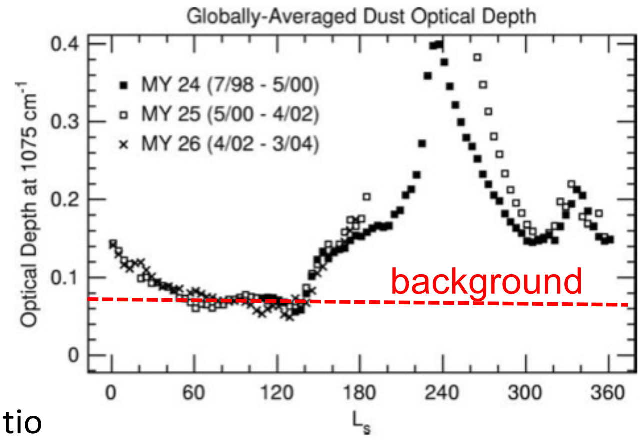

Meridional distribution of dust mixing ratio

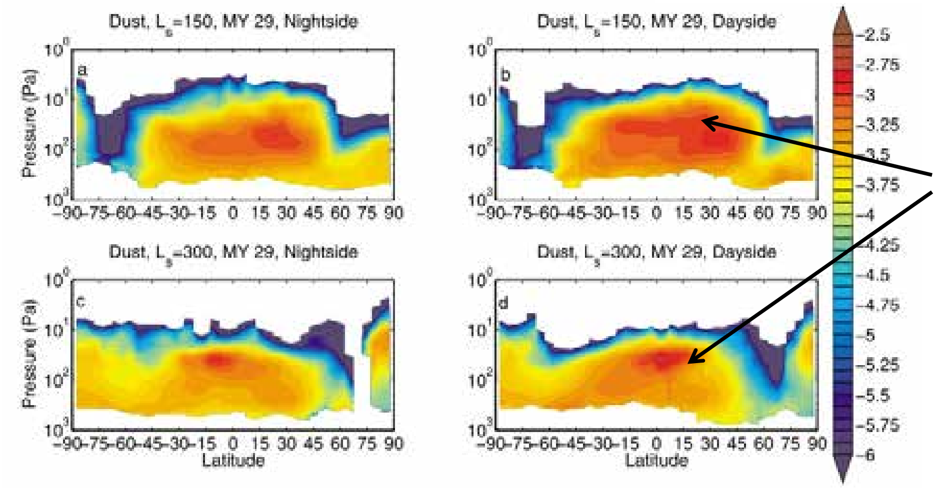

Heavens et al. (2011)

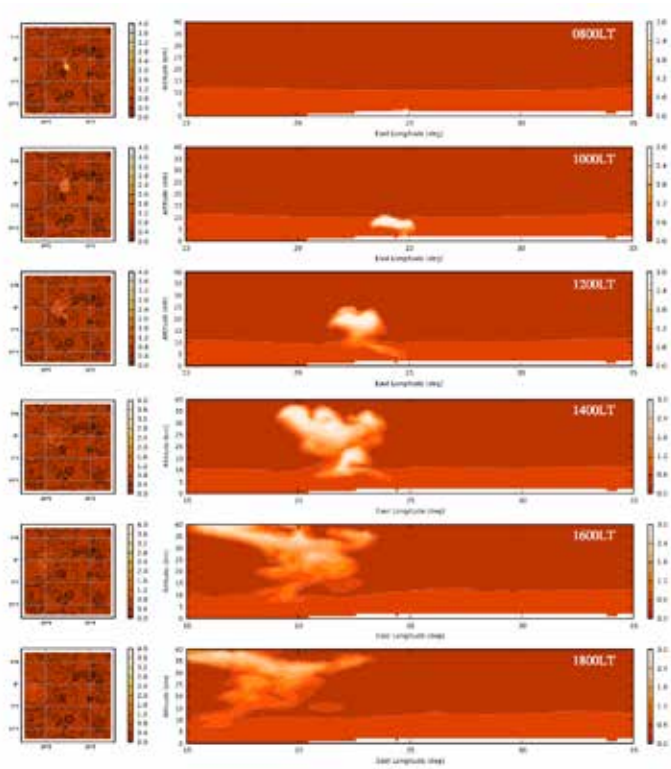

Figure 12. The LMD-MMM storm simulation with lifting and no initial dust perturbation. Same as Figure 4 except that local times range from 0800 to 1800 and longitude-altitude sections are obtained at latitude 1.5°S.

“Rocket dust storm”

Modeling by Spiga et al. (2013)

Dust plumes continuously get buoyancy through solar heating

H_2O ice clouds on Mars

HST Mars image

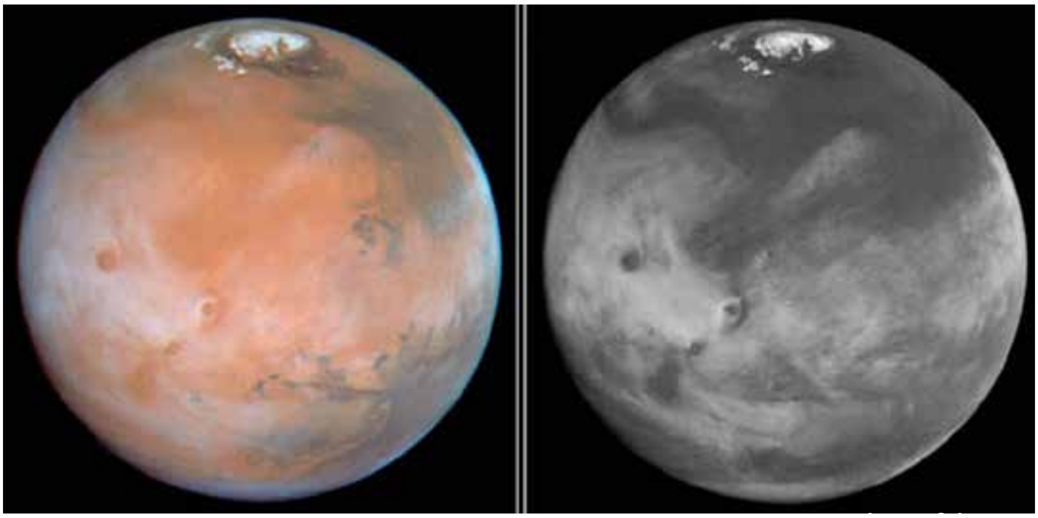

color composite   blue (410 nm)

Seasonal variation of dust, clouds, and H_2O vapor observed by an infrared spectrometer (TES) on Mars Global Surveyor

Dust

Ice clouds

Water vapor

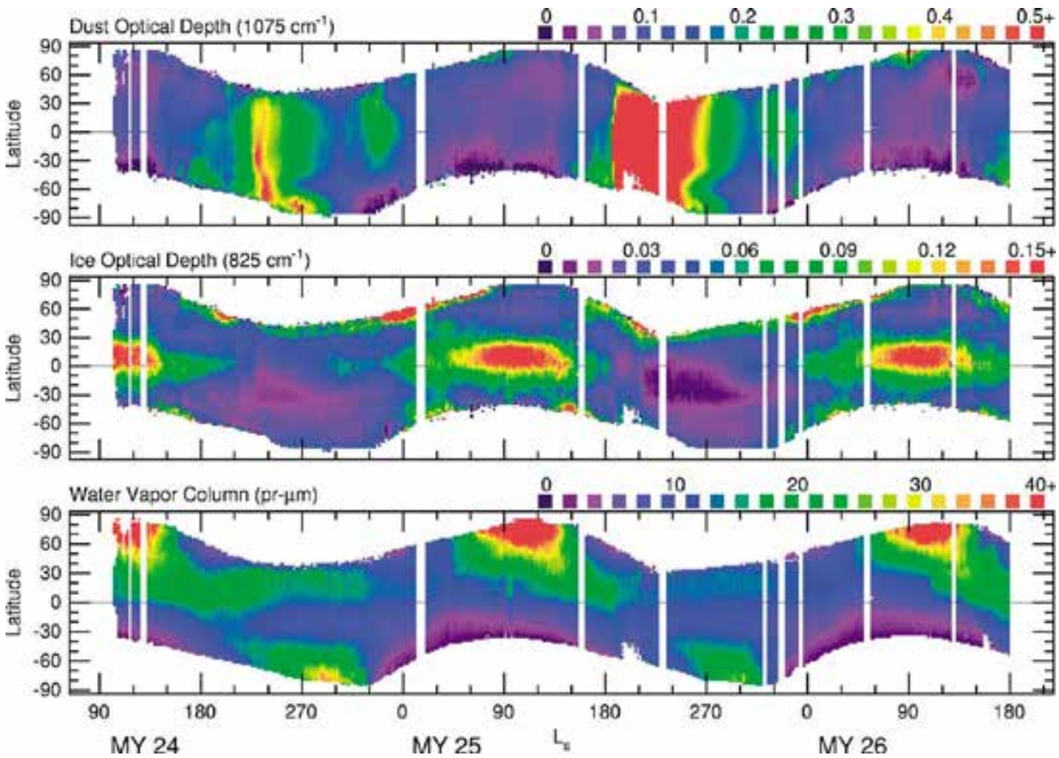

Smith, Icarus 167 (2004) 148–165

Seasonal cycle of Martian water

- 北極冠の消長が全体を駆動
- 北半球の春～夏に北極冠が昇華して北極域の水蒸気濃度が上昇、これが(この時期の弱い)水平渦で低緯度に拡散的に運ばれる。
- 低緯度に運ばれた水蒸気の一部は赤道越えのハドレー循環で南半球へ
- 北半球の秋～冬には北極冠で凝結により水蒸気濃度が低下し、南北濃度勾配が逆転するため、傾圧不安定などに伴う水平渦で低緯度から北極域に水蒸気が拡散的に戻る。低緯度の水蒸気量はそれまでの水蒸気輸送の履歴で決まる。

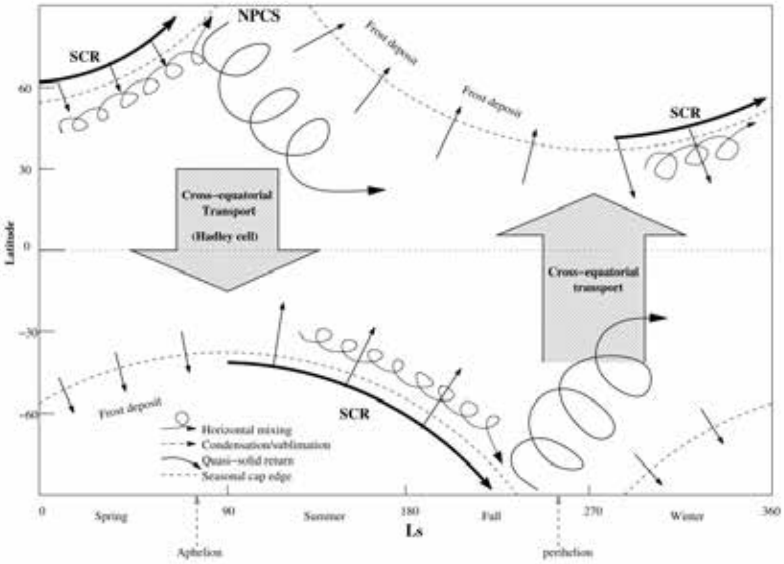

Figure 3. Chart describing the principal events affecting the Martian water cycle over the course of a year. NPCS stands for North Polar Cap Sublimation; SCR stands for Seasonal Cap Recession.

Water transport by Hadley circulation

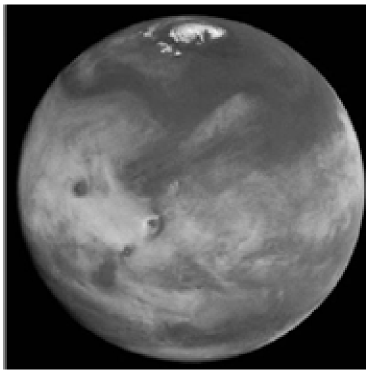

- Warmer southern summer than northern favors net northward transport of water.

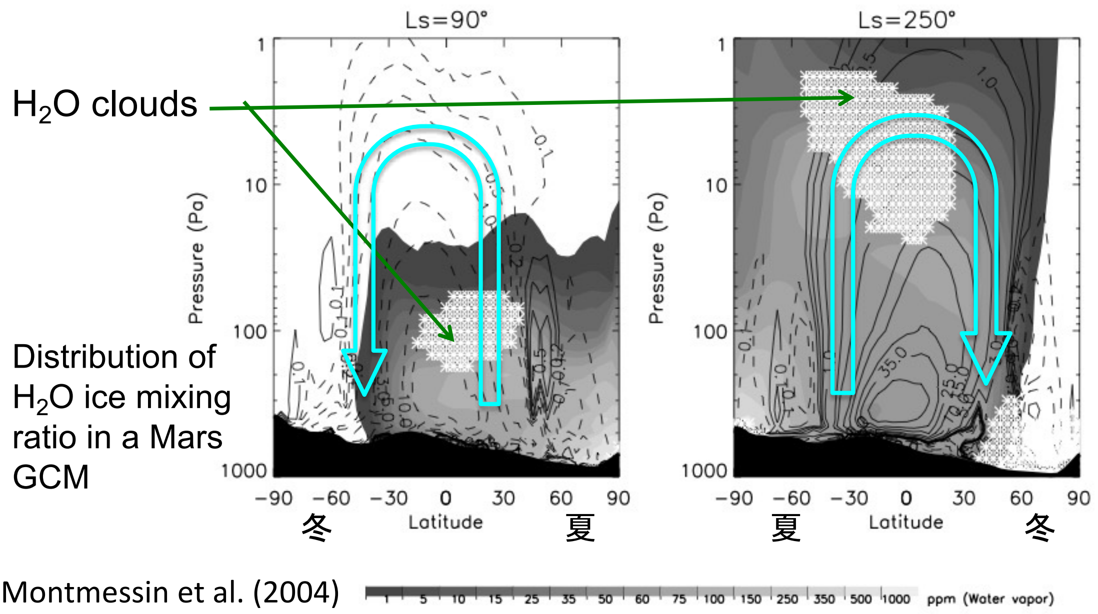

Montmessin et al. (2004)

Supersaturation of water vapor on Mars

SPICAM on Mars Express (Maltagliati et al. 2011)

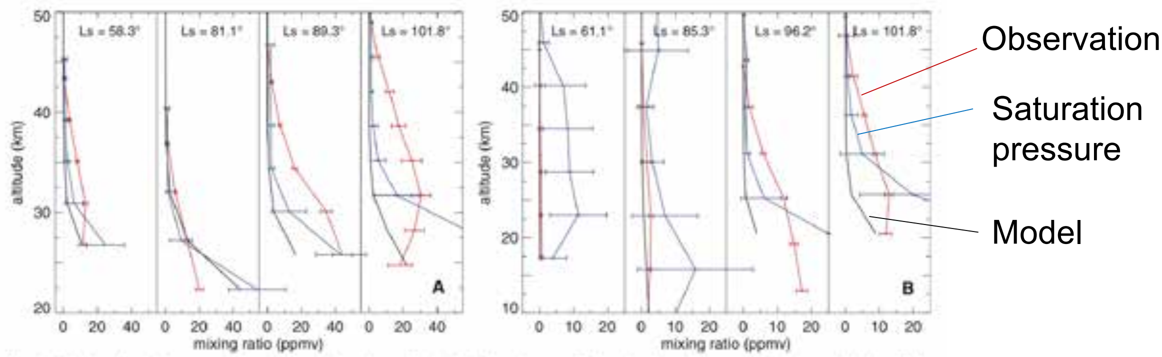

Fig. 2. Selection of typical water vapor volume–mixing ratio profiles in the (**A**) northern and (**B**) southern hemisphere. Black curve, modeled profile by the LMD-GCM; red curve, the retrieved SPICAM results; blue curve, saturation water vapor–mixing ratio. Supersaturation exists where the red values are greater than the blue ones.

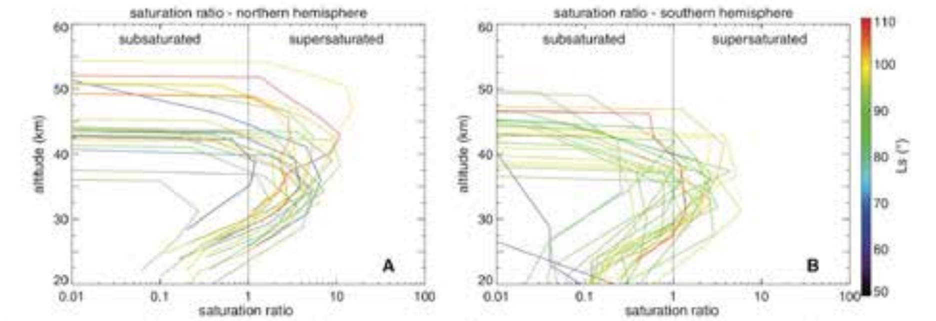

Fig. 3. Saturation ratio for all orbits of the campaign. (**A**) Northern hemisphere. (**B**) Southern hemisphere. The vertical line marks the value of 1, which corresponds to the saturated state.

Dependence of volatile escape on lower atmosphere processes

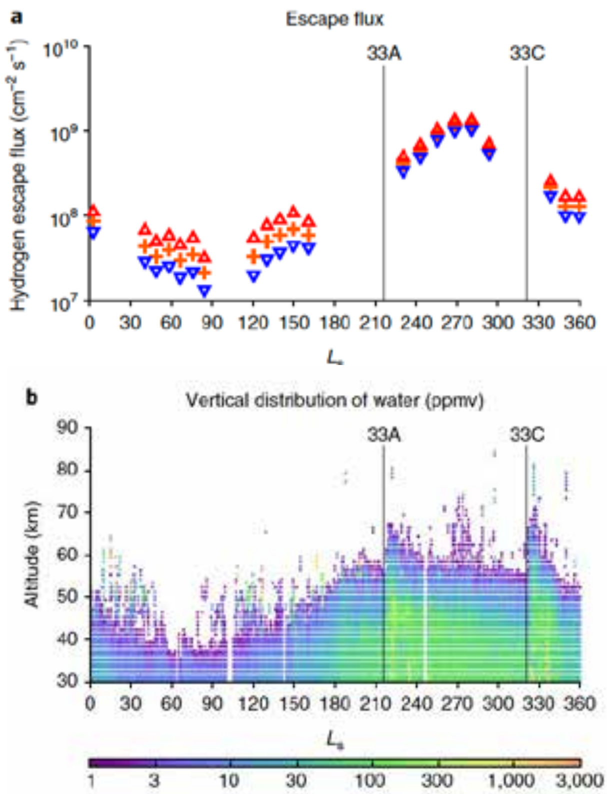

Hydrogen escape measured by MAVEN
Solar Wind Ion Analyzer

Vertical distribution of total water content measured by MRO MCS

Heavens et al. (2018)

Meridional distribution of zonal-mean temperature obtained by MGS/TES (Smith et al. 2001)

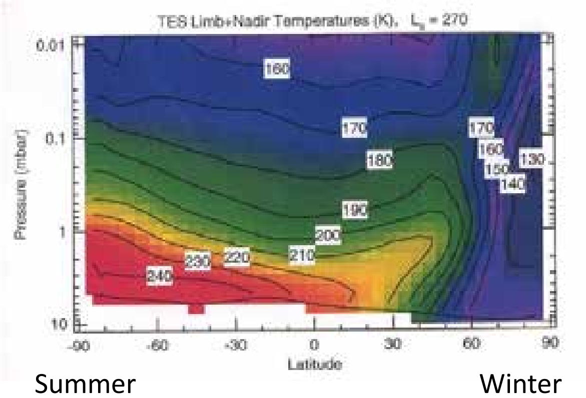

Summer Winter

Meridional cross sections in Mars GCM (Shaposhnikov et al. 2019)

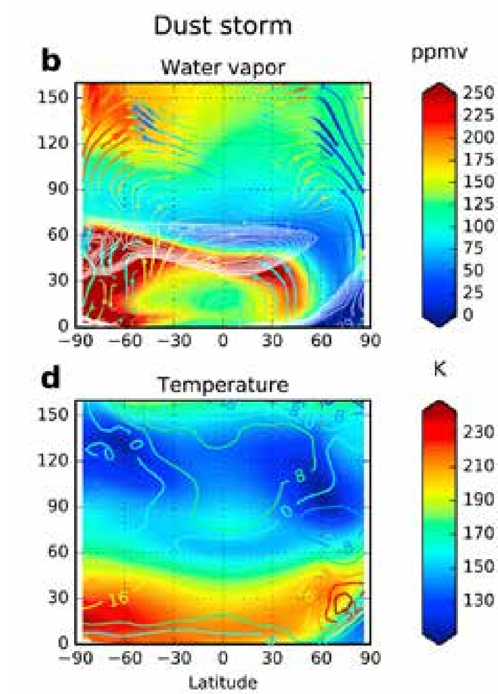

Traditional scheme New concept

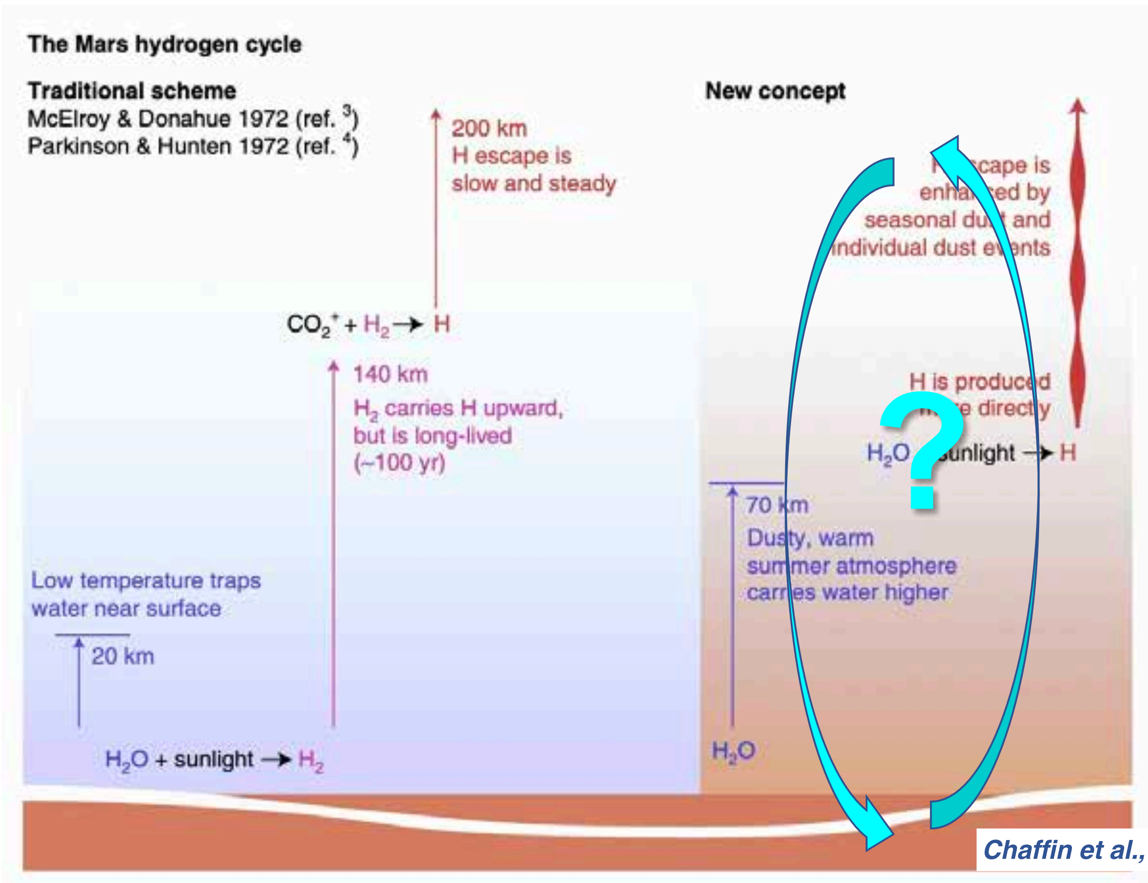

Chaffin et al., 2021

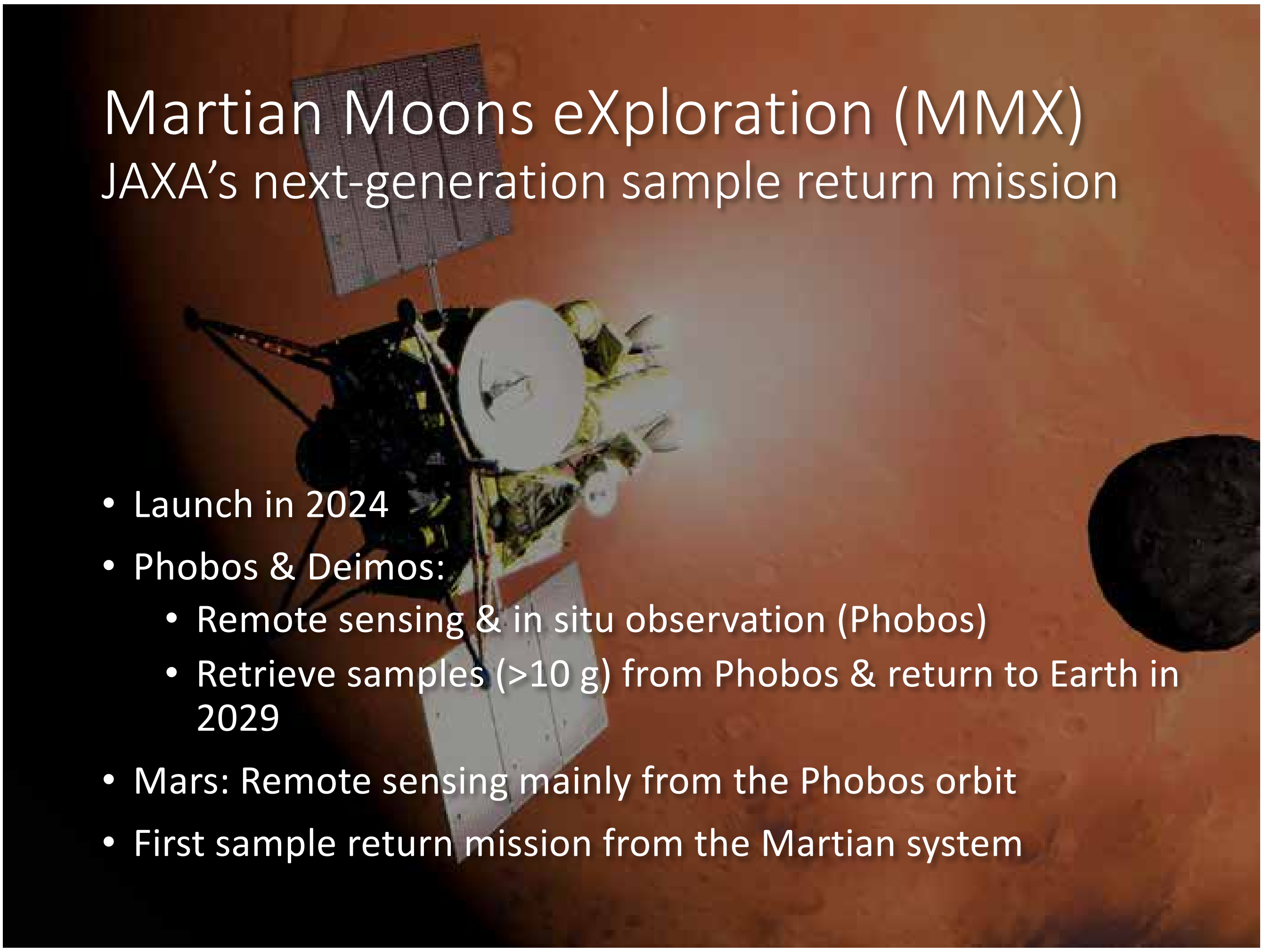

Martian Moons eXploration (MMX)
JAXA's next-generation sample return mission

- Launch in 2024
- Phobos & Deimos:
  - Remote sensing & in situ observation (Phobos)
  - Retrieve samples (>10 g) from Phobos & return to Earth in 2029
- Mars: Remote sensing mainly from the Phobos orbit
- First sample return mission from the Martian system

Instruments for Mars atmosphere observation

- **OROCHI**
  - Wide-angle camera, 8 colors
  - 3 colors (480, 650, 950 nm) will be used for Mars observation.
  - 2.5 km/pix (sub S/C) from QSO
- **TENGOO**
  - Narrow-angle camera
  - 35 m/pix (sub S/C) from QSO
- **MIRS**
  - Push-bloom type spectrometer
  - Spectral resolution: 10nm
  - Spectral bandpass: 0.9–3.6 μm
  - 2.1 km/pix (sub S/C) from QSO

Kameda et al. (2021)

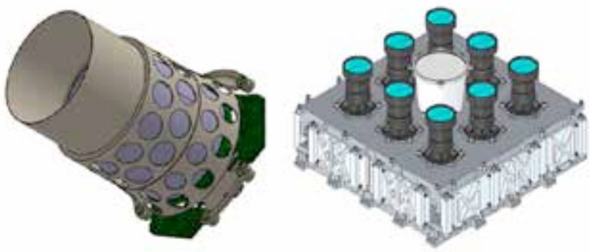

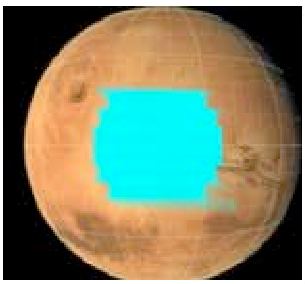

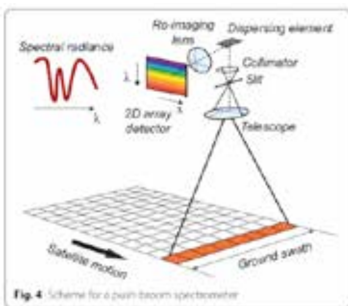

Barucci et al. (2021)

Continuous global monitoring from Martian orbit

High-altitude equatorial orbit is a unique platform for atmospheric studies

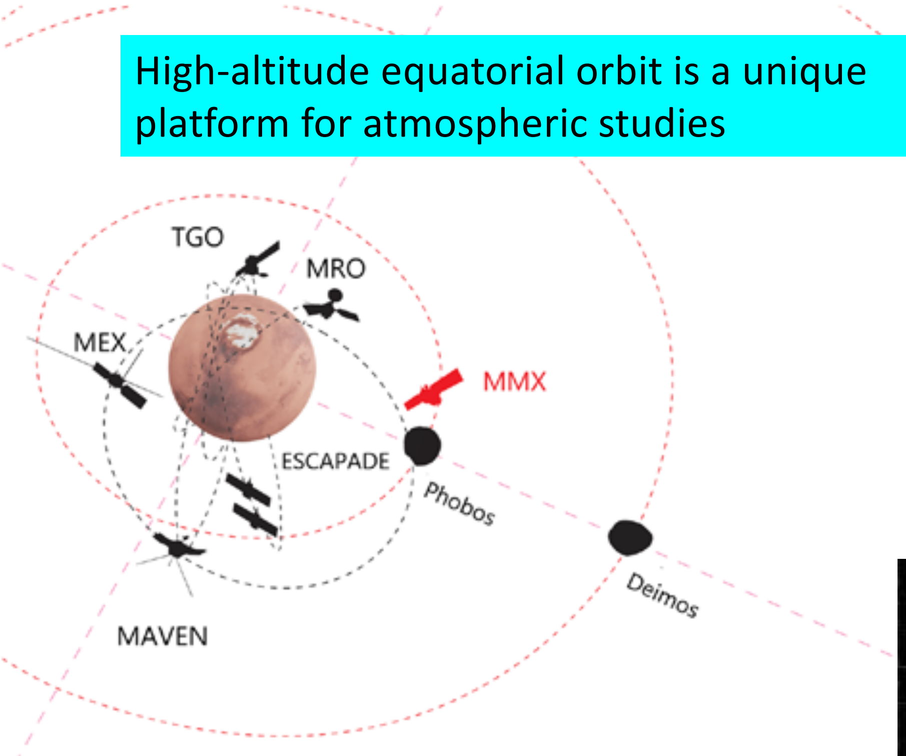

Ogohara et al. (2022)

Venus images taken by JAXA's Akatsuki

UV

IR

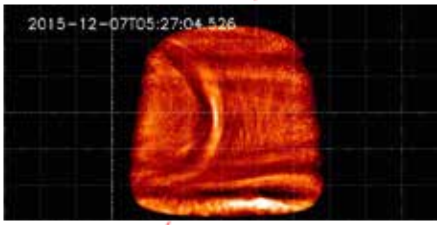

Chemistry of gas giants

Many of the gases observed in their atmospheres are hydrides, which are thermodynamically stable forms in the H_2-rich atmospheres (e.g., CH_4, NH_3, H_2O, H_2S, PH_3, GeH_4, and AsH_3).

These gases (except H_2O and H_2S) are photochemically destroyed by solar UV in the stratosphere to produce disequilibrium species (e.g., C_2H_6, C_2H_2, C_2H_4, N_2H_4).

The disequilibrium species react with H_2 to reform hydrides once they are transported downward into the hot, high pressure regions.

Lodders, 2010

Table 2. *Composition of the Atmospheres of Jupiter, Saturn, Uranus, and Neptune*

Gas	Jupiter[a]	Saturn	Uranus	Neptune
$\boxed{H_2}$	86.4 ± 0.3%	88 ± 2%	~82.5 ± 3.3%	~80 ± 3.2 %
^4He	13.6 ± 0.3%	12 ± 2%	15.2 ± 3.3 %	19.0 ± 3.2 %
$\boxed{CH_4}$	$(1.81 \pm 0.34) \times 10^{-3}$	$(4.7 \pm 0.2) \times 10^{-3}$	~2.3 %	~1-2 %
$\boxed{NH_3}$	$(6.1 \pm 2.8) \times 10^{-4}$	$(1.6 \pm 1.1) \times 10^{-4}$	<100 ppb	<600 ppb
H_2O	520^{+340}_{-240} ppm	2–20 ppb		
H_2S	67 ± 4 ppm	<0.4 ppm	<0.8 ppm	<3 ppm
HD	45 ± 12 ppm	110 ± 58 ppm	~148 ppm	~192 ppm
$^{13}CH_4$	19 ± 1 ppm	51±2 ppm		
C_2H_6	5.8 ± 1.5 ppm	7.0 ± 1.5 ppm		
PH_3	1.1 ± 0.4 ppm	4.5 ± 1.4 ppm		
CH_3D	0.20 ± 0.04 ppm	0.30 ± 0.02 ppm	~8.3 ppm	~12 ppm
C_2H_2	0.11 ± 0.03 ppm	0.30 ± 0.10 ppm	~10 ppb	60^{+140}_{-40} ppb
HCN	60 ± 10 ppb	<4 ppb	<15 ppb	0.3 ± 0.15 ppb
HC_3N			<0.8 ppb	<0.4 ppb
C_2H_4	7 ± 3 ppb	~0.2 ppb[b]		
CO_2	5-35 ppb	0.3 ppb	40 ± 5 ppt	
C_2H_6			10 ± 1 ppb	$1.5^{+2.5}_{-0.5}$ ppm
CH_3C_2H	2.5^{+2}_{-1} ppb	0.6 ppb	0.25 ± 0.03 ppb	
CO	1.6 ± 0.3 ppb	1.4 ± 0.7 ppb	<40 ppb	0.65 ± 0.35 ppm
CH_3CN				<5 ppb
GeH_4	$0.7^{+0.4}_{-0.2}$ ppb	0.4 ± 0.4 ppb		
C_4H_2	0.3 ± 0.2 ppb	0.09 ppb	0.16 ± 0.02 ppb	
AsH_3	0.22 ± 0.11 ppb	2.1 ± 1.3 ppb		

[a] ^3He 22.6±0.7 ppm, Ne 21±3 ppm, Ar 16±3 ppm, Kr 8±1 ppb, Xe 0.8±0.1 ppb.
[b] assuming a total stratospheric column density of 1.54%10^{25} cm^{-2}.
From Lodders & Fegley 1998 and updates: Mahaffy et al. 2000, Atreya et al. 2003, Lodders 2004, Wong et al. 2004

Cycle of hydrogen-bearing species on giant planets

Catling & Kasting (2017)

$$2CH_4 + \text{photons} \rightarrow \underbrace{C_2H_6 + H_2}_{\text{ethane + hydrogen}}$$

$$2nCH_4 + \text{photons} \rightarrow \underbrace{(C_2H_2)_n + 3nH_2}_{\text{polyacetylene + hydrogen}}$$

$$6nCH_4 + \text{photons} \rightarrow \underbrace{(C_6H_6)_n + 9nH_2}_{\text{polyaromatic hydrocarbons + hydrogen}}$$

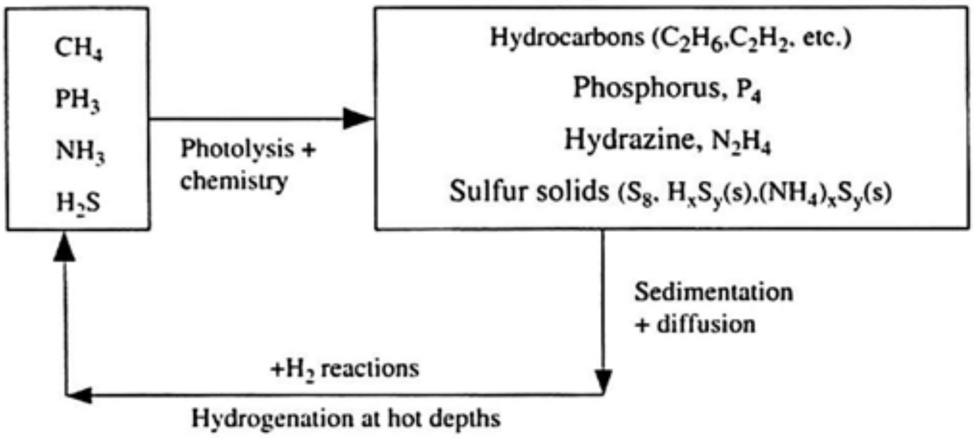

Clouds

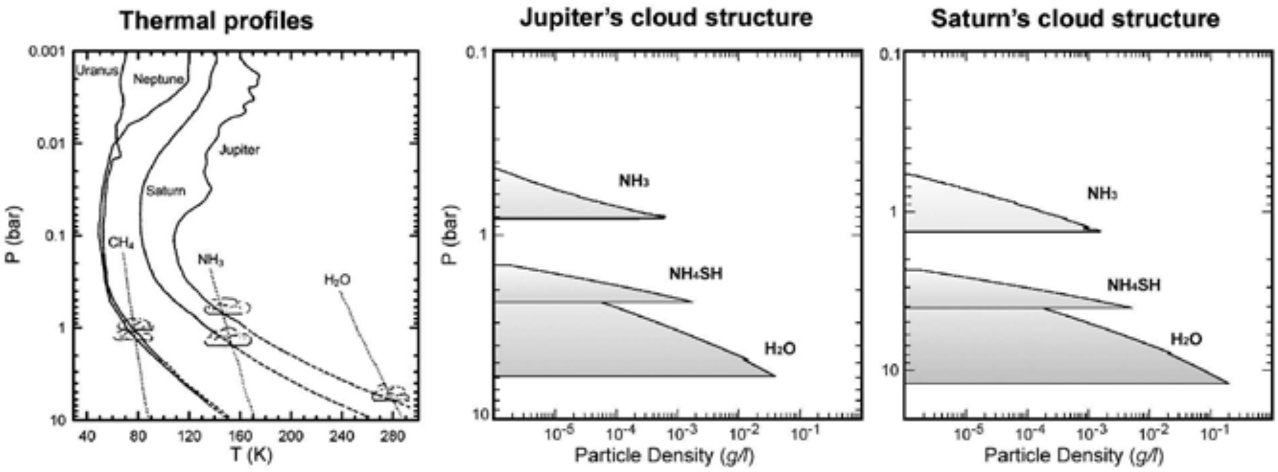

Sanchez-Lavega et al.

Galileo probe (entry: December 7, 1995)

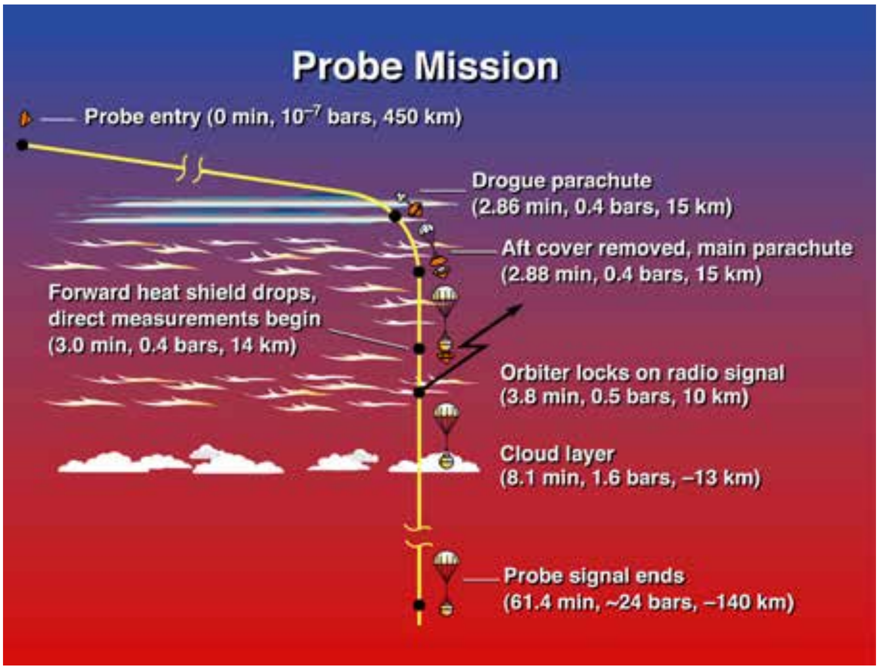

©NASA

Dry atmosphere ?

- Brightness of the sky abruptly drops off at a pressure level of 0.6 bars, indicating an ammonia cloud layer above this height. Clouds were *not* seen below.
- Clouds are patchy and that the Probe went through a relatively clear area.
- The atmosphere has much less oxygen than the Sun's atmosphere, implying a surprisingly dry atmosphere.
- Oxygen was expected to be enriched relative to the solar value due to impacts by comets and other small bodies over the 4.5 billion years.

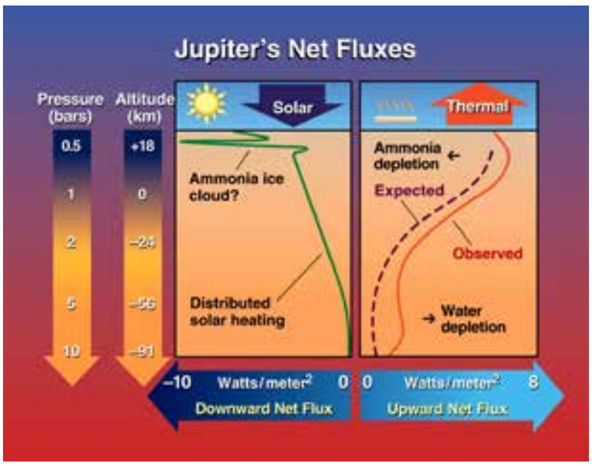

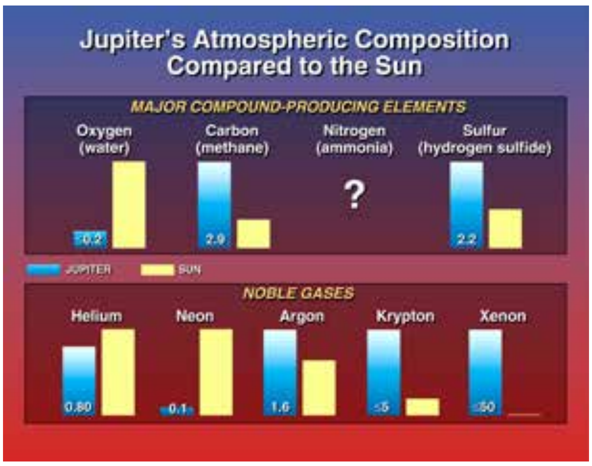

©NASA

The probe apparently entered a special location

The Probe entry site is near the edge of a so-called infrared "**hot spot**". These "hot spots" are believed to represent regions of diminished clouds on Jupiter.

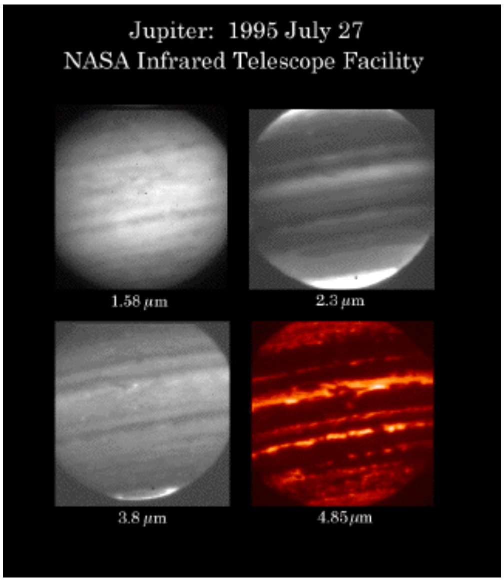

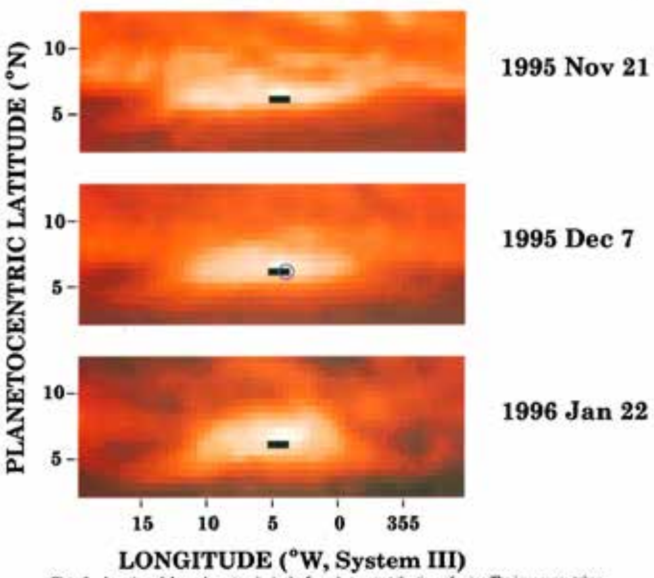

Plate 3. Location of the probe entry site in the 5-μm hot spot at the time of entry. The images are taken from the upper panel of Plate 2 and, again, scaled to the brightest pixel in each image. A single 0.5° × 0.5° pixel is used to denote the 6.5°N planetocentric latitude and System III longitude of the probe entry, and a 1.5° longitude (three-pixel) extent depicts the longitudinal extent of the probe entry path, starting from 350 km above the 1-bar level to the 1-bar level and deeper (as in Figures 1 and 2 of *Orton et al.* [1996]). A 1-σ circle shows the effects of the pointing uncertainty on the location of the final portion of the probe entry. The panels from different dates were aligned together using a drift rate of 103 m/s relative to System III.

Orton et al. 1998

Atmospheric chemistry on Titan

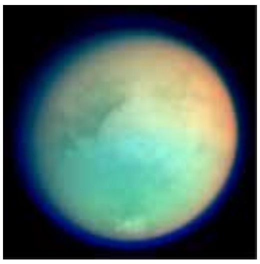

Atmospheric composition of Titan (Coustenis 2007)

Constituent	Mole Fraction (atm. altitude level)
Major	
Molecular nitrogen, N_2	0.98
Methane, CH_4	4.9×10^{-2} (surface)
	$1.4–1.6 \times 10^{-2}$ (stratosphere)
Monodeuterated methane, CH_3D	6×10^{-4} (in CH_3D, in stratosphere.)
Argon, ^{36}Ar	2.8×10^{-7}
^{40}Ar	4.3×10^{-5}
Minor	
Hydrogen, H_2	~0.0011
Ethane, C_2H_6	1.5×10^{-5} (around 130 km)
Propane, C_3H_8	5×10^{-7} (around 125 km)
Acetylene, C_2H_2	4×10^{-6} (around 140 km)
Ethylene, C_2H_4	1.5×10^{-7} (around 130 km)
Methylacetylene, CH_3C_2H	6.5×10^{-9} (around 110 km)[a]
Diacetylene, C_4H_2	1.3×10^{-9} (around 110 km)[a]
Cyanogen, C_2N_2	5.5×10^{-9} (around 120 km)[a]
Hydrogen cyanide, HCN	1.0×10^{-7} (around 120 km)[a]
	5×10^{-7} (around 200 km)[b]
	5×10^{-6} (around 500 km)[b]
Cyanoacetylene, HC_3N	1×10^{-9} (around 120 km)[c]
	1×10^{-7} (around 500 km)[b]
Acetonitrile, CH_3CN	1×10^{-8} (around 200 km)[c]
	1×10^{-7} (around 500 km)
Water, H_2O	8×10^{-9} (at 400 km)[d]
Carbon monoxide, CO	4×10^{-5} (uniform profile)[e]
Carbon dioxide, CO2	1.5×10^{-8} (around 120 km)

Vuitton et al. (2014)

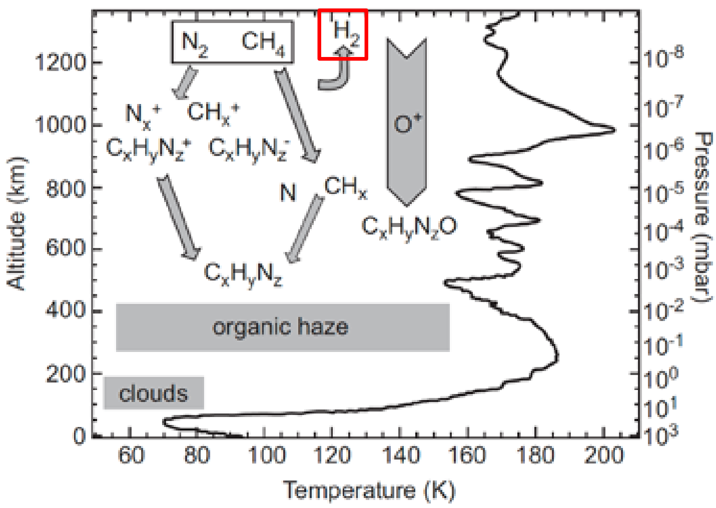

Titan

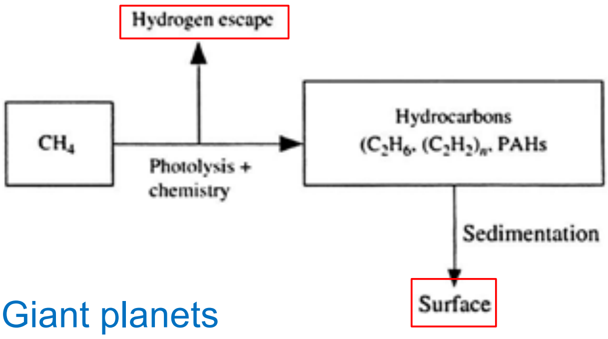

Giant planets

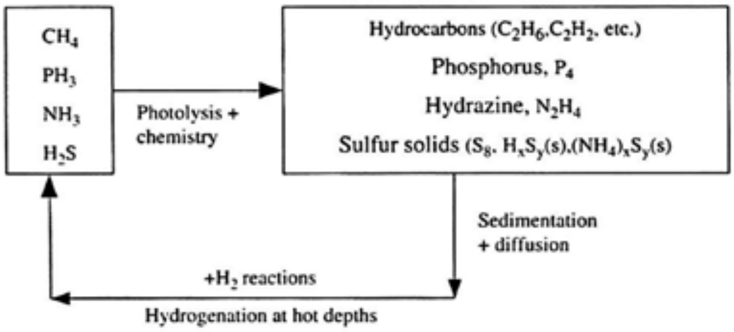

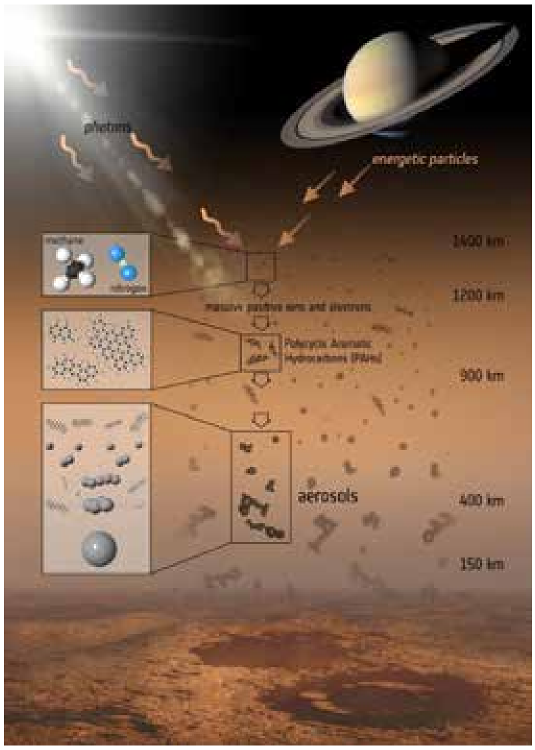

© NASA

Catling & Kasting (2017)

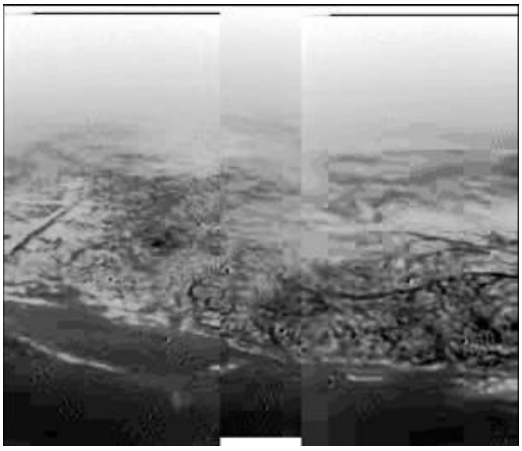

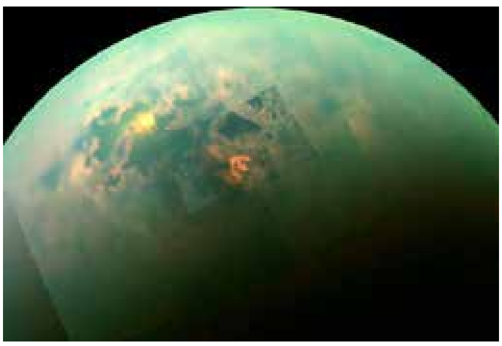

Cassini's Visual and Infrared Mapping Spectrometer (VIMS)

Huygens' touchdown